AFRL-AFOSR-VA-TR-2018-0407

Probing Biotic/Abiotic Interfaces at the Nanoscale using Limited Proteolysis and Chiral Plasmonics

Srikanth Singamaneni
WASHINGTON UNIVERSITY THE

10/09/2018
Final Report

Air Force Research Laboratory
AF Office Of Scientific Research (AFOSR)/ RTB2
Arlington, Virginia 22203
Air Force Materiel Command

REPORT DOCUMENTATION PAGE

Form Approved
OMB No. 0704-0188

1. REPORT DATE *(DD-MM-YYYY)*	**2. REPORT TYPE**	**3. DATES COVERED** *(From - To)*
06/09/2018	Final	06/15/2015-06/14/2018

4. TITLE AND SUBTITLE
Probing Biotic/Abiotic Interfaces at the Nanoscale using Limited Proteolysis and Chiral Plasmonics

5a. CONTRACT NUMBER

5b. GRANT NUMBER
FA9550-15-1-0228

5c. PROGRAM ELEMENT NUMBER

6. AUTHOR(S)
Srikanth Singamaneni

5d. PROJECT NUMBER

5e. TASK NUMBER

5f. WORK UNIT NUMBER

7. PERFORMING ORGANIZATION NAME(S) AND ADDRESS(ES)
Washington University,
1 Brookings Dr.,
Saint Louis MO 63130-4862

8. PERFORMING ORGANIZATION REPORT NUMBER

9. SPONSORING/MONITORING AGENCY NAME(S) AND ADDRESS(ES)
AF OFFICE OF SCIENTIFIC RESEARCH
875 North Randolph St., Rm 3112
Arlington VA 22203-1954

10. SPONSOR/MONITOR'S ACRONYM(S)

11. SPONSOR/MONITOR'S REPORT NUMBER(S)

12. DISTRIBUTION/AVAILABILITY STATEMENT
Distribution A

13. SUPPLEMENTARY NOTES

14. ABSTRACT

The ultimate goal of the project is to acquire a better understanding of biotic/abiotic interface at the nanoscale that enables us to precisely engineer the interface between a biomolecule and a synthetic nanostructure, leading to rapid advances in the field of bio/nano hybrids. We investigated the influence of size, curvature and charge of the nanostructures on the structure and biocatalytic activity of bionanoconjugates. The structure and biocatalytic activity of the enzyme was found to be highly dependent on the charge and surface curvature of the nanostructures.

15. SUBJECT TERMS

16. SECURITY CLASSIFICATION OF:			**17. LIMITATION OF ABSTRACT**	**18. NUMBER OF PAGES**	**19a. NAME OF RESPONSIBLE PERSON**
a. REPORT	**b. ABSTRACT**	**c. THIS PAGE**			**19b. TELEPHONE NUMBER** *(Include area code)*

INSTRUCTIONS FOR COMPLETING SF 298

1. REPORT DATE. Full publication date, including day, month, if available. Must cite at least the year and be Year 2000 compliant, e.g. 30-06-1998; xx-06-1998; xx-xx-1998.

2. REPORT TYPE. State the type of report, such as final, technical, interim, memorandum, master's thesis, progress, quarterly, research, special, group study, etc.

3. DATE COVERED. Indicate the time during which the work was performed and the report was written, e.g., Jun 1997 - Jun 1998; 1-10 Jun 1996; May - Nov 1998; Nov 1998.

4. TITLE. Enter title and subtitle with volume number and part number, if applicable. On classified documents, enter the title classification in parentheses.

5a. CONTRACT NUMBER. Enter all contract numbers as they appear in the report, e.g. F33315-86-C-5169.

5b. GRANT NUMBER. Enter all grant numbers as they appear in the report. e.g. AFOSR-82-1234.

5c. PROGRAM ELEMENT NUMBER. Enter all program element numbers as they appear in the report, e.g. 61101A.

5e. TASK NUMBER. Enter all task numbers as they appear in the report, e.g. 05; RF0330201; T4112.

5f. WORK UNIT NUMBER. Enter all work unit numbers as they appear in the report, e.g. 001; AFAPL30480105.

6. AUTHOR(S). Enter name(s) of person(s) responsible for writing the report, performing the research, or credited with the content of the report. The form of entry is the last name, first name, middle initial, and additional qualifiers separated by commas, e.g. Smith, Richard, J, Jr.

7. PERFORMING ORGANIZATION NAME(S) AND ADDRESS(ES). Self-explanatory.

8. PERFORMING ORGANIZATION REPORT NUMBER. Enter all unique alphanumeric report numbers assigned by the performing organization, e.g. BRL-1234; AFWL-TR-85-4017-Vol-21-PT-2.

9. SPONSORING/MONITORING AGENCY NAME(S) AND ADDRESS(ES). Enter the name and address of the organization(s) financially responsible for and monitoring the work.

10. SPONSOR/MONITOR'S ACRONYM(S). Enter, if available, e.g. BRL, ARDEC, NADC.

11. SPONSOR/MONITOR'S REPORT NUMBER(S). Enter report number as assigned by the sponsoring/ monitoring agency, if available, e.g. BRL-TR-829; -215.

12. DISTRIBUTION/AVAILABILITY STATEMENT. Use agency-mandated availability statements to indicate the public availability or distribution limitations of the report. If additional limitations/ restrictions or special markings are indicated, follow agency authorization procedures, e.g. RD/FRD, PROPIN, ITAR, etc. Include copyright information.

13. SUPPLEMENTARY NOTES. Enter information not included elsewhere such as: prepared in cooperation with; translation of; report supersedes; old edition number, etc.

14. ABSTRACT. A brief (approximately 200 words) factual summary of the most significant information.

15. SUBJECT TERMS. Key words or phrases identifying major concepts in the report.

16. SECURITY CLASSIFICATION. Enter security classification in accordance with security classification regulations, e.g. U, C, S, etc. If this form contains classified information, stamp classification level on the top and bottom of this page.

17. LIMITATION OF ABSTRACT. This block must be completed to assign a distribution limitation to the abstract. Enter UU (Unclassified Unlimited) or SAR (Same as Report). An entry in this block is necessary if the abstract is to be limited.

Award#: FA9550-15-1-0228

Title: Probing Biotic/Abiotic Interfaces at the Nanoscale using Limited Proteolysis and Chiral Plasmonics

Project Period: June 15th 2015-June 14th 2018

PI: Srikanth Singamaneni, Department of Mechanical Engineering and Materials Science; Washington University in St. Louis, 1 Brookings Dr., St. Louis, MO 63130; Ph.: 314-935-5407; singamaneni@wustl.edu

Project goal and specific objectives

The ultimate goal of the project is to acquire a better understanding of biotic/abiotic interface at the nanoscale that enables us to precisely engineer the interface between a biomolecule and a synthetic nanostructure, leading to rapid advances in the field of bio/nano hybrids. Specific objectives include:

- Synthesis of representative abiotic nanostructures with well-defined physicochemical characteristics (e.g., size, shape, composition, crystal planes, and surface chemistry)
- Identify the binding site and orientation of a few model proteins (e.g., enzymes) adsorbed on size-, shape-, and surface chemistry-controlled nanostructures.
- Probe the changes in the secondary structure of the enzymes adsorbed on model abiotic nanostructures and correlate the changes in the structure to the variations in their biocatalytic activity.
- Monitor the binding kinetics at ensemble and individual nanoparticle level to reveal the possible cooperative mechanism in the binding process using size-, shape- and surface chemistry-controlled plasmonic nanostructures.
- Study the adsorption behavior of multi-domain structural proteins on nanomaterials with a complex distribution of chemical functionality to realize advanced bionanocomposites.
- Devise strategies to interface functional proteins with optically-active nanostructures and preserve the biofunctionality of the nanoconjugates under extreme conditions.
- Devise strategies to interface optically-active nanostructures with biofoams to realize 3D optically-active bionanocomposites.

Major accomplishments

- We investigated the influence of size, curvature and charge of the nanostructures on the structure and biocatalytic activity of bionanoconjugates. The structure and biocatalytic activity of the enzyme was found to be highly dependent on the charge and surface curvature of the nanostructures.
- We have designed Au superstructures to deconvolute the effects of differential diffusion of the nanostructures and the local curvature on the observed catalytic efficiency of the bionanoconjugates. We found that Michaelis–Menten constant (K_M) is more sensitive to surface curvature of the nanostructure than the overall hydrodynamic size of the nanostructure. On the other hand, turnover number (K_{cat}) directly scaled with the hydrodynamic size of the bionanoconjugates.
- We introduced a simple and highly effective strategy to stabilize enzymes immobilized on plasmonic nanostructures by encapsulating them through *in situ* polymerization. Apart from enhanced thermal and biological stability, the encapsulation strategy provides enhancement in the enzyme activity with an

external optical trigger. The encapsulation strategy demonstrated here can be a highly attractive approach for designing remote-controlled biomolecular reactions.

- We have also demonstrated metal-organic framework as highly efficient exoskeletons for preserving the functionality of biomolecules conjugated to plasmonic nanostructures and the ability to control the biomolecular reactions with external optical trigger.
- We have investigated silk and metal-organic frameworks (MOFs) as protective coatings for preservation of biorecognition abilities of antibodies conjugated to plasmonic nanostructures. We found that MOF-encapsulated antibodies retain their biorecognition abilities even after subjecting them to extreme denaturing conditions such as 60° C for 2 weeks.
- We have extended the MOF-based biopreservation to preserve the structure and functionality of various biomarkers in biofluids such as urine, serum and plasma.

Selected detailed examples of studies conducted

Biocatalytic activity of bionanoconjugates

We have investigated the effect of surface charge of abiotic nanostructures on the biocatalytic activity of bionanoconjugates. We found that the surface charge on the nanostructures profoundly influences the activity of the bound enzyme suggesting that the biomolecular structure at the interface is dependent on the surface charge of the nanostructure. AuNPs coated with positively-charged (poly-(allylamine) hydrochloride, (PAH) and negatively-charged *poly-(styrene-sulfonate*) (PSS)) are used as model charge-controlled nanostructures. The zeta potential of PSS coated AuNP (PSS-AuNP) and PAH coated AuNP (PAH-AuNP) was found to about -45 mV and +58 mV, respectively. Polyelectrolyte-coated AuNP exhibited excellent colloidal stability and distinct zeta potentials (-45 mV and +58 mV) making them excellent candidates for studying the effect of surface charge of the nanostructures on the binding site accessibility and biocatalytic activity of bionanoconjugates. We employed horseradish peroxidase (HRP) as the model enzyme to probe the influence of surface charge of the nanostructures on the biocatalytic activity of the bionanoconjugates. HRP is one of the most widely studied peroxidase that is extensively used in various bioanalytical applications. he dimensions of HRP are known to be 3.0 × 6.5 × 7.5 nm and the isoelectric point (pI) of HRP is 7.2.[1] Considering that the adsorption of HRP on charge-controlled AuNPs was performed at pH 5.2, the enzyme should possess a net positive charge under these conditions. The adsorption of HRP on AuNPs results in a red shift in the localized surface plasmon resonance (LSPR) wavelength of the nanostructures, an increase in the hydrodynamic diameter and a change in the zeta potential, the magnitudes of which depend on the surface chemistry of the nanostructures (Figure 1(A-D)). The adsorption of HRP on PSS-AuNP resulted in a red shift of ~4 nm and an increase in hydrodynamic diameter by ~6.4 nm (Figure 1A, C). PAH-NPs showed an LSPR wavelength shift of ~2 nm and an increase in hydrodynamic diameter of ~4 nm upon the adsorption of HRP (Figure 1B, C). Taken together, HRP forms a monolayer on both PSS-AuNP and PAH-AuNP. The significantly lower LSPR shift and a smaller increase in hydrodynamic diameter of PAH-AuNP compared to PSS-AuNP is possibly due to the significantly larger degree of unfolding and spreading of HRP on PAH-AuNP. In the case of PSS-AuNP, the adsorption of HRP on the negatively charged nanoparticles creates little disruption to the native conformation due to the accessible

positively charged lysine and arginine residues on the surface of the HRP interacting with negatively charged nanostructures. [2]

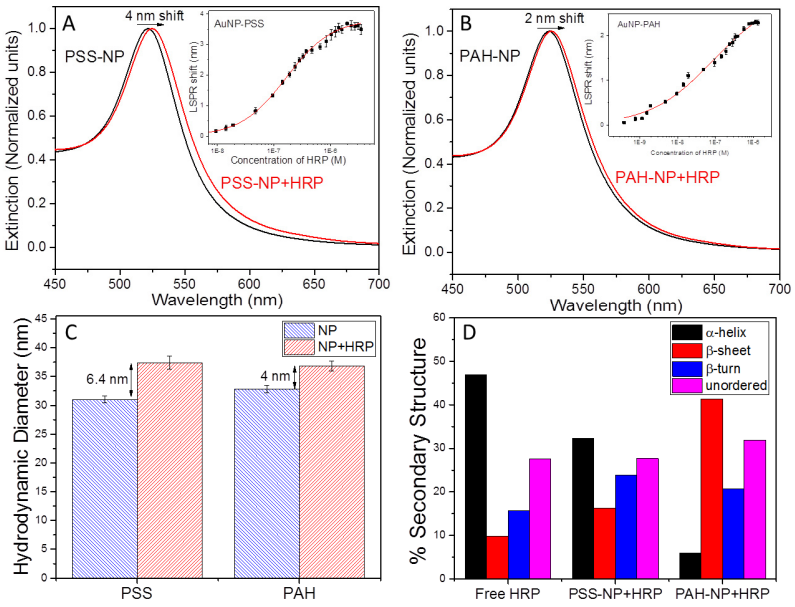

Figure 1: Extinction Spectra of AuNPs showing a shift in the LSPR wavelength upon coating with (A) PSS and (B) PAH. Inset shows the LSPR shift as a function of HRP concentration. (C) Plot showing the hydrodynamic diameter of polyelectrolyte coated nanostructures. (D) Secondary structure content of free HRP and HRP adsorbed on AuNP surface with different surface coatings.

In order to understand the activity of HRP adsorbed on nanoparticles with different surface chemistries, we measured the enzyme kinetics of NP-HRP conjugates using 2,2'-azino-bis(3-ethylbenzothiazoline-6-sulphonic acid) (ABTS) as the substrate (Figure 2(A-B)).[3] The enzyme kinetic parameters of the NP-HRP conjugates were found to be dependent on the charge of the nanostructures (Figure 2(D-F)). The turnover number (k_{cat}) of NP-HRP conjugates for PAH-NPs was found to be ~40 times higher than that of PSS-NPs. Although the adsorption of HRP is favored on PSS-NPs, the activity of the enzyme bound on negatively charged PSS-NPs is significantly lower compared to that bound on positively charged PAH-NPs due to the masking of the active site of the enzyme. The lower activity of the PSS-NP bioconjugates compared to PAH-AuNP bioconjugates is possibly due to the difference in the binding orientation of HRP on the differentially charged nanostructures. The interacting sites of HRP with negatively charged PSS occur through the positively charged arginine and lysine (Arg-302 and Lys-65) at the surface, which preserve the secondary structure preventing the denaturation. Furthermore, the positively charged residues Arg-38 and His-42 around the active site most likely form a favorable docking site on negatively charged PSS-NPs through electrostatic interactions (Figure 2C).[4] Binding of HRP on PSS-AuNP with the active site orientated towards the nanoparticle surface significantly reduces the accessibility of the active site to the substrate, effectively lowering the catalytic activity. In case of PAH-NPs, the relative positions of the negatively charged residues Asp-81, Asp-66 and Asp-56 do not prevent the accessibility to the active site due to the presence of positively charged residues in the pocket. We believe that the mechanism of inhibition for

PSS-NPs is through the masking of the active site of the enzyme preventing the substrate molecules to bind with the active site.

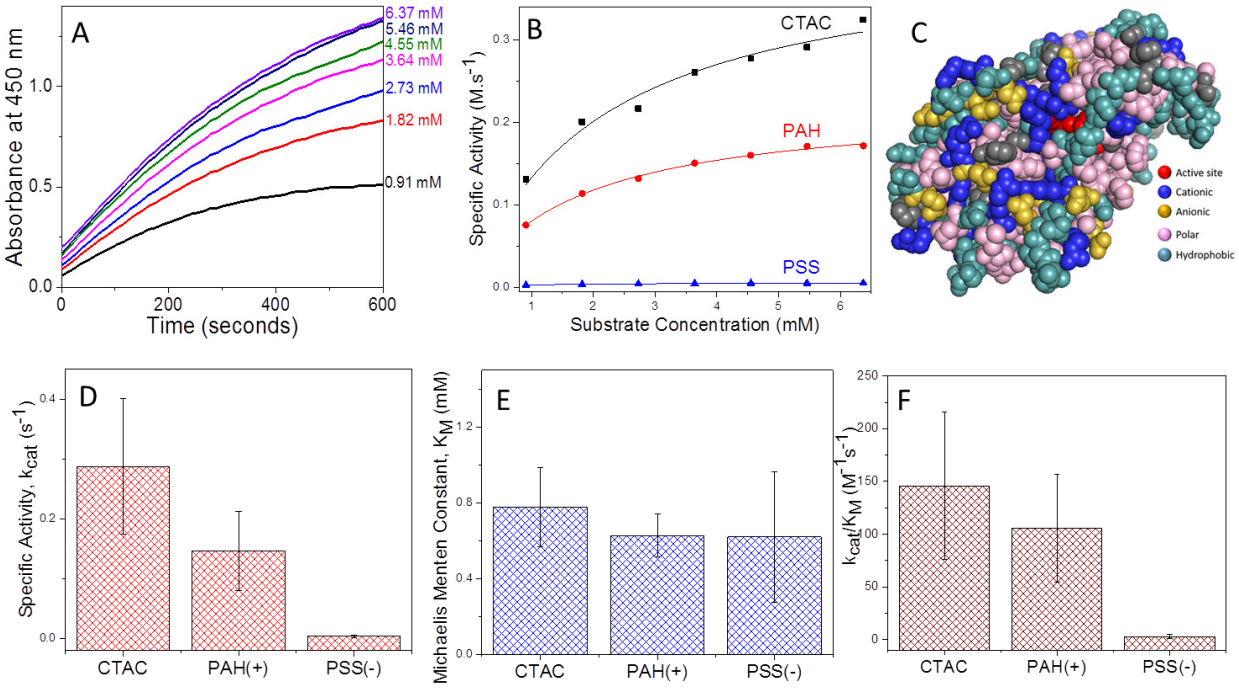

Figure 2: (A) Time dependent absorption of ABTS during the catalysis with PAH-NP+HRP measured at 450 nm at different concentrations of ABTS. Inset: Schematic showing the mechanism of the ABTS assay used in the study. (B) Activity of bionanoconjugates with different functionalities normalized to the concentration of HRP in the conjugates. (C) Space-filling model of HRP representing the functionally significant residues. (D) The catalytic constant k_{cat} (E) Michaelis-Menten constant and (F) catalytic efficiency (k_{cat}/K_M) of bionanoconjugates with different surface charge.

From our studies, we conclude that the catalytic activity of the bionanoconjugates is dominated by the accessibility of the active site rather than the degree of change in the secondary structure of the enzyme adsorbed on the nanostructure. This study improves our fundamental understanding of the bio-nano interface and the design of bioinorganic hybrids with synergistic and enhanced properties with applications in biomimetic and bioenabled sensors, energy harvesting structures, optoelectronic components and devices, responsive and autonomous materials. The concerted non-specific interactions at the bio-nano interface enable us to design bio-nano conjugates that have a significantly higher resistance to thermal denaturation when compared to their free counterparts.

Effect of Size and Curvature on the Enzyme Activity of Bionanoconjugates

Biotic-abiotic hybrids comprised of globular proteins and functional nanostructures with complementary and synergistic properties are central to a number of bionanotechnological applications. A comprehensive understanding of the effect of physicochemical properties of abiotic nanostructures on

the biological activity of the bionanoconjugates is critical in the design of these bio-nano hybrids. In this study, using size and curvature-controlled gold nanoparticles as a model abiotic system, we investigated the effect of hydrodynamic diameter and surface curvature on the activity of a model enzyme, horseradish peroxidase (HRP), adsorbed on the surface of the nanostructures. In contrast to the previous studies, we have employed a novel class of gold superstructures (gold nanoparticles on spheres) to deconvolute the effects of size and curvature on the catalytic activity of the bionanoconjugates.

To understand the activity of HRP adsorbed on size-controlled nanoparticles, we measured the enzyme kinetics of NP-HRP conjugates (Figure 3(A-B)). The enzyme kinetics of NP-HRP conjugates exhibited a Michaelis-Menten behavior as depicted in Figure 1A, B.[5] The rate of product formation at different substrate concentrations is fit using Michaelis-Menten equation given by:[6]

$$V_o = \frac{V_{max}\,[S]}{K_M + [S]}$$

Where V_o is the rate of the reaction, V_{max} is maximum rate of the reaction at saturating substrate concentration, [S] is the substrate concentration, and K_M is the Michaelis-Menten constant, which represents the inverse of the enzyme affinity to the substrate. The catalytic constant k_{cat} (turnover number), given by, $k_{cat} = \frac{V_{max}}{[E_t]}$ where E_t is the total enzyme concentration, is used to determine the catalytic efficiency, C_{eff}, of the enzyme, given by $C_{eff} = \frac{k_{cat}}{K_M}$.

We have measured the k_{cat} and K_M of size-controlled NP-HRP conjugates to understand the effects of enzyme kinetics on the nanoparticle size and curvature. We have observed that the k_{cat} of the NP-HRP conjugates reduces with the increase in the size of the bionanoconjugates (Figure 3C). The turnover number k_{cat}, represents the number of substrate molecules converted into the product by the enzyme per second. We attribute the drop in the turnover number of the NP-HRP conjugates to the increase in the nanoparticle size and slower diffusion kinetics of the bionanoconjugates in the reaction solution when compared to the free enzyme.

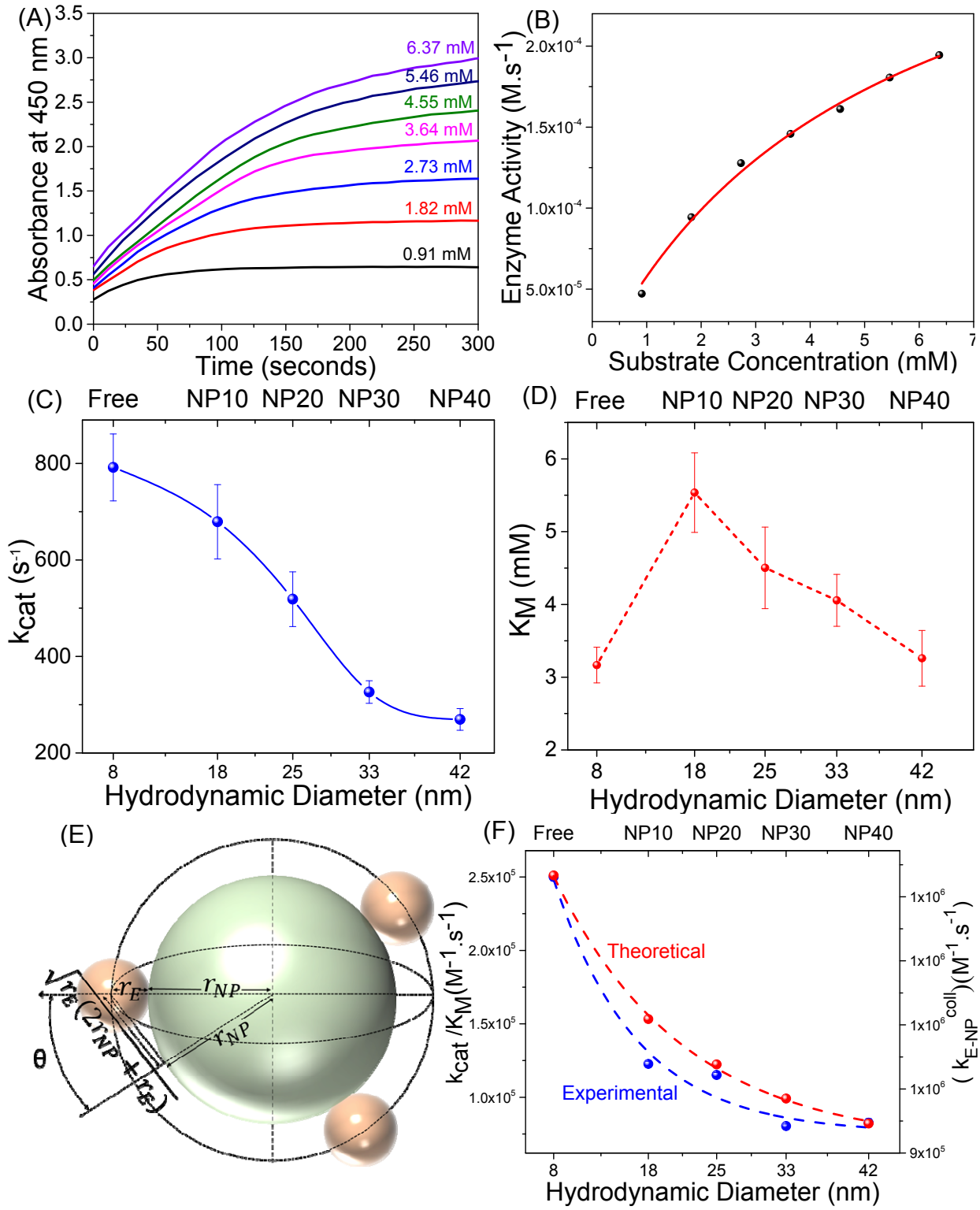

Figure 3: (A) Representative colorimetric biocatalytic activity of NP20-HRP conjugates at different concentrations of the substrate (ABTS) (B) Enzyme activity obtained from the slope of the absorbance at different substrate concentrations. (C) Turnover number (k_{cat}) of free HRP and NP+HRP conjugates.

(D) Michaelis-Menten constant (K_M) as a function of the hydrodynamic diameter of the nanoparticle. (E) Schematic depicting the parameters involved in the theoretical model. (F) Plot showing the catalytic efficiency of free and size-controlled bionanoconjugates in comparison to the theoretical model.

The Michaelis-Menten constant (K_M) of the NP10 was found to higher compared to that of the free enzyme (Figure 3D). This is due to the reduction in the accessibility of the active site to the substrate molecules in the NP10-HRP conjugates due to the local steric hindrance imposed by the adjacent enzymes on the nanoparticles. However, as the particle size increased, we observed a drop in the K_M. A careful examination of the adsorption suggests that the free volume available on the NP-HRP conjugates increases with the increase in the particle size. This suggests a possible crowding effect at high surface curvatures due to which the accessibility of the active site reduces resulting in higher K_M values for smaller NPs. As the surface curvature reduces, a higher degree of unfolding of HRP alleviates the crowding of the enzymes resulting in more accessibility of the active site and lower K_M values (Figure 3D).

We employed diffusion-collision theory to understand the experimentally observed variations in the catalytic efficiency of the bionanoconjugates with varying hydrodynamic diameter.[7] In particular, a hard sphere model was used to model the reaction kinetics of the free enzyme and nanoconjugate (Figure 3E). The biocatalytic reaction rate depends on the concentrations of the enzyme and substrate and a biomolecular rate constant k_{coll} given by,[7]

$$k_{coll} = Z.p.\eta.e^{(\frac{-E_A}{RT})}$$

where Z is the frequency of the collisions between the enzyme and the substrate and p is the steric factor that accounts for a specific relative orientation for enzyme-substrate effective collision and η is the solid angle fraction of the enzyme surface bound on a nanostructure open to the substrate. By using diffusion-collision theory and Stokes-Einstein relation, the maximum collision frequency of effective collisions for enzyme-NP conjugates is given by [7]

$$k_{E-NP}^{coll} = \frac{RT(r_E + r_S)}{1500\mu}\left(\frac{1}{r_{E-NP}} + \frac{1}{r_S}\right)(r_E + r_S).\eta.e^{-(\frac{E_A}{RT})}$$

Where

$$\eta = \frac{\Omega}{4\pi} = \frac{1}{2}\left(1 + \frac{\sqrt{r_E(2r_{NP}+r_E)}}{r_{NP}+r_E}\right)$$

We used this theoretical model to calculate the biomolecular rate constant, k_{E-NP}^{coll} and compare with the experimentally obtained catalytic efficiency values (k_{cat}/K_M) (Figure 3F). Notably, the biomolecular rate constant, k_{E-NP}^{coll} obtained from diffusion-collision theory follows a similar trend as the experimentally observed catalytic efficiency values (k_{cat}/K_M). It is important to note that the theoretical model employed here does not account for the changes in the secondary structure upon adsorption of the enzyme on nanostructures and consequent variations in the catalytic efficiency of the bionanoconjugates. The discrepancy between the experimental and those obtained from the above model is attributed to the crowding of the enzyme on the nanoparticle and the loss in secondary structure of the enzyme after adsorption to the nanoparticle which are not accounted for in the theoretical model. Although the hydrodynamic diameter-dependent catalytic efficiency values effectively capture the size-dependent diffusion of the bionanoconjugates, it does not deconvolute the effects of size and curvature of the nanostructure on the biocatalytic activity.

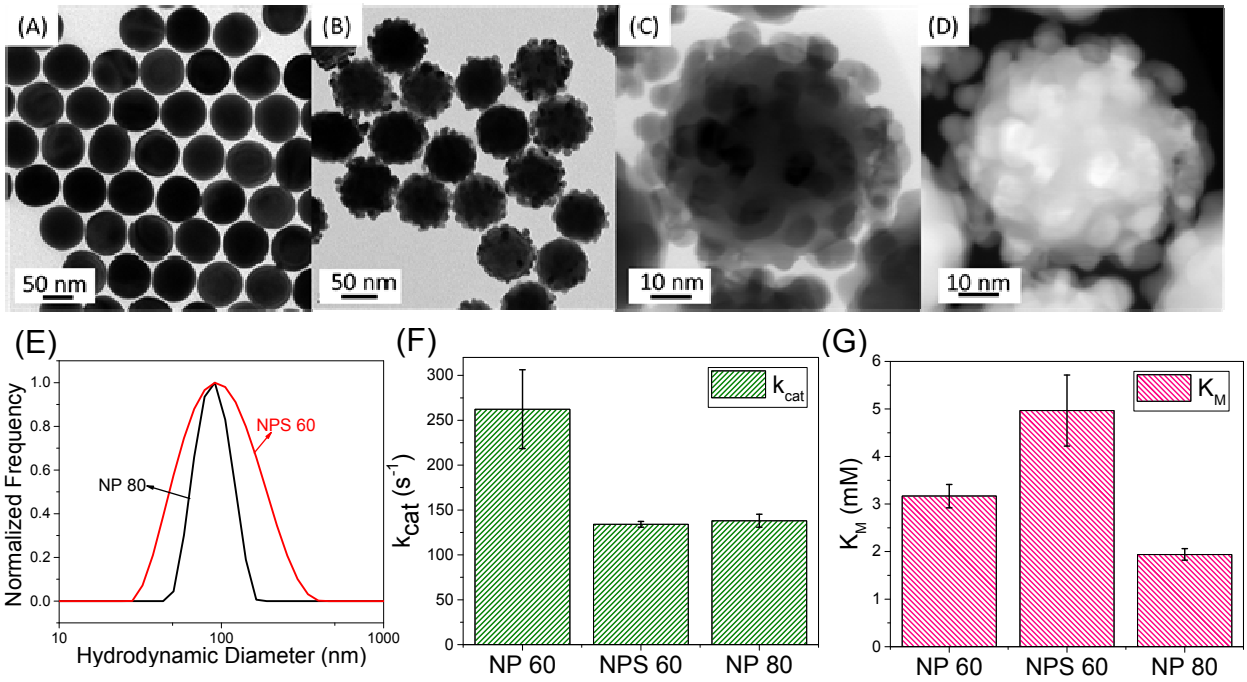

Figure 4: (A) Representative TEM image of 80 nm AuNPs. (B,C) Bright field TEM images of 60 nm AuNPS. (D) High angle angular dark field (HAADF) image of 60 nm AuNPS. (E) Hydrodynamic diameter of 80 nm AuNP and 60 nm AuNPS (F, G) Plot showing the k_{cat} and K_M values of 60 nm NP, 60 nm NPS and 80 nm NP.

We note that the catalytic activity of the NP-HRP conjugates depends on two major factors, i) hydrodynamic size of the bionanoconjugates effecting the diffusion of the bionanoconjugates and ii) nanoparticle curvature-dependent loss in the secondary structure of the enzyme and local steric hindrances imposed by the adjacent enzymes on the nanostructure. In order to distinguish these two effects, we have used a novel class of nanostructures called gold nanoparticles on spheres (AuNPS).[8-9] The AuNPS is comprised of 10 nm Au nanoparticles grown on a 60 nm Au nanosphere (Figure 4 A, B). These superstructures (AuNPS) when compared to 80 nm AuNP exhibit the same hydrodynamic diameter but a significantly higher local curvature due to the presence of 10 nm nanoparticles (Figure 4C, D). By using the same capping agent, we have controlled the surface chemistry of the nanostructures such that they exhibit similar zeta potential and the only distinguishing feature is the local curvature. By employing these two nanostructures, we aim to deconvolute the effects of variation in hydrodynamic size and local curvature in order to better understand these effects on the biocatalytic properties of bionanoconjugates.

We found that the k_{cat} values of NP60 is higher than that of the NPS60 and NP80, which can be attributed to the higher diffusion rates associated with the NP60 due to the smaller size (Figure 4F). The k_{cat} values of the NPS60 and NP80 were found to be comparable suggesting that the k_{cat} is significantly influenced by the hydrodynamic diameter of the nanoparticles. Although, the secondary structure of enzyme on the NPS60 is slightly better preserved when compared to that on NP80, it did not result in a significant difference in the measured turnover numbers (k_{cat}) of these two bionanoconjugates. The expected higher K_{cat} of NPS60 compared to NP80 due to better preserved

secondary structure of enzyme on NPS60 is possibly negated by the longer times scales associated with the substrate molecules accessing the active site of the enzyme adsorbed in between the curved features of the NPS60 as opposed to the NP80. Interestingly, we noted a significantly higher K_M for NPS60 compared to that of NP60 and NP80 (Figure 4G). The higher value of K_M in NPS60, comparable to that of NP10, is due to the limited accessibility of the substrate to the active site attributed to the high surface curvature in these two cases. This finding suggests that K_M is more sensitive to surface curvature of the nanostructure than the overall hydrodynamic size of the nanostructure.

Photothermal Enhancement of Biocatalytic Activity of Polymer Encapsulated Enzyme

Photothermal ability of plasmonic nanostructures is highly attractive to optically modulate biomolecular processes such as biocatalysis. However, the studies pertaining to the phothermal enhancement of enzyme activity are limited to thermophilic enzymes due to the thermal denaturation and loss in the activity of conventional enzymes at elevated temperatures. The lack of effective strategies for preserving the activity of immobilized enzymes at elevated temperatures hinders the potential use of plasmonic nanostructures as nanoheaters for the photothermal enhancement of enzyme activity. Here, we demonstrate a simple and highly effective strategy to stabilize enzymes immobilized on plasmonic nanostructures by encapsulating them through *in situ* polymerization. Apart from enhanced thermal and biological stability, the encapsulation strategy provides enhancement in the enzyme activity with an external optical trigger. The encapsulation strategy demonstrated here can be a highly attractive approach for designing remote-controlled biomolecular reactions.

We used gold nanorods (AuNR) as optically-excitable nanoscale heating elements for the immobilization of enzymes. AuNRs with a length of 63.5±1.5 nm and a diameter of 12.2±0.5 nm are synthesized using a seed-mediated approach (Figure 5B).[10] The adsorption of HRP on the AuNR resulted in a red-shift in the localized surface plasmon resonance (LSPR) wavelength corresponding to the increase in the refractive index of the medium surrounding AuNR (Figure 5C). The bionanoconjugate solution is filtered to remove the unconjugated HRP. The filtered bionanoconjugates are uniformly adsorbed on a glass substrate. The adsorbed AuNR-HRP substrates are catalytically active as verified by a colorimetric assay based on 2,2'-azino-bis (3-ethylbenzothiazoline-6-sulphonic acid) (ABTS).

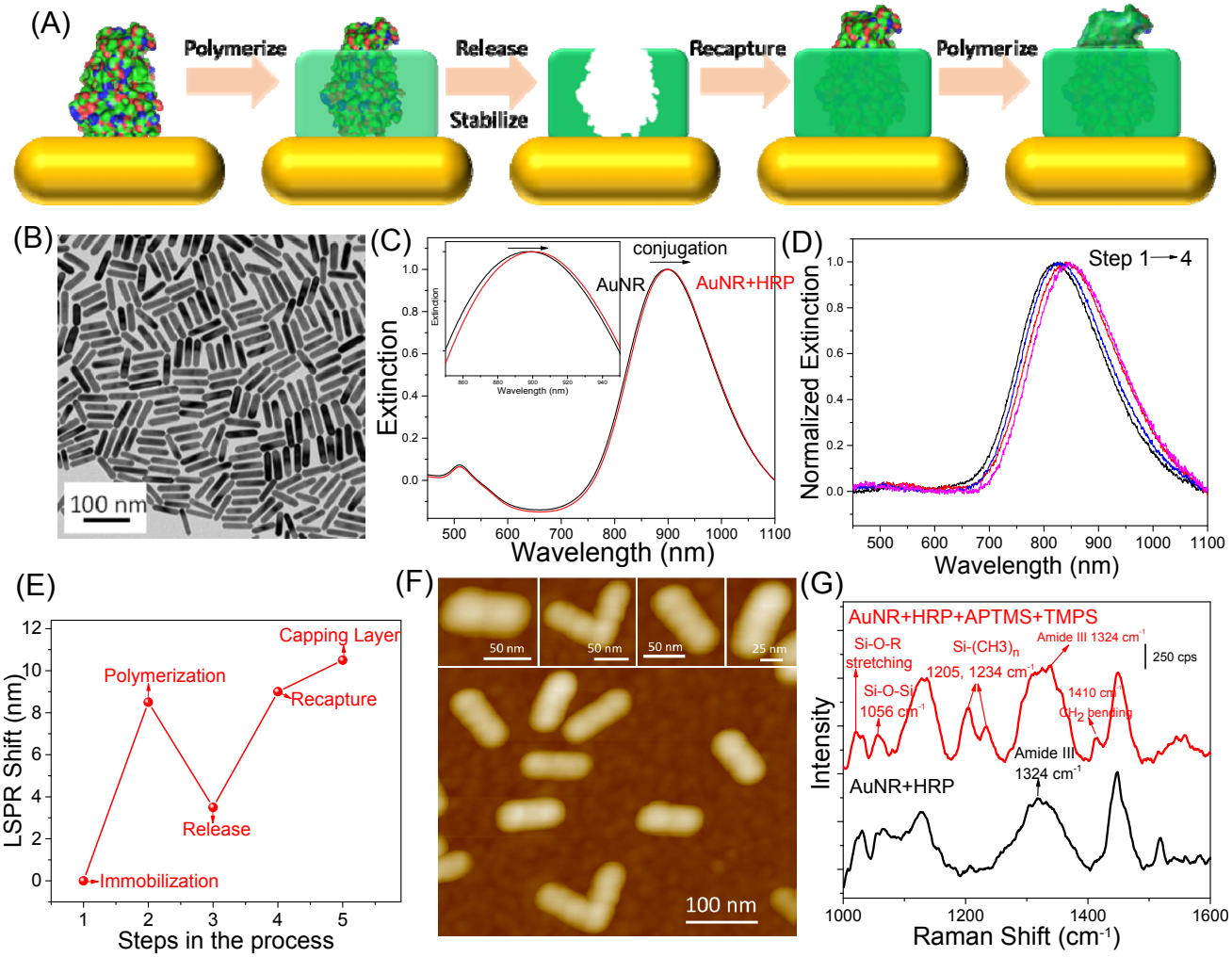

Figure 5: (A) Schematic illustration showing the polymer encapsulation strategy for enzyme stabilization. (B) Representative TEM image of AuNRs employed in this study. (C) Extinction spectrum of AuNRs showing a red shift in the LSPR wavelength after adsorption of HRP. (D) Extinction spectra of AuNRs following each step in the polymer encapsulation process. (E) LSPR wavelength shift of each step during the polymer encapsulation process showing the release and recapture of the enzyme. (F) AFM image of the polymer encapsulated enzyme adsorbed on the AuNRs. (G) Raman characterization of the AuNR+HRP conjugates before and after polymerization showing the characteristic peaks.

Figure 5A shows the various steps involved in the organosilica-based preservation of biocatalytic activity of bionanoconjugates. Following the immobilization of the bionanoconjugates on a glass substrate, an organosilica encapsulation layer is formed through copolymerization of trimethoxypropyl silane (TMPS) and (3-aminopropyl) trimethoxysilane (APTMS) around the AuNR-HRP surface. The ethoxy group of APTMS and the methoxy group of the TMPS undergo rapid hydrolysis to form ethanol, methanol and trisilanols.[11] Due to the subsequent condensation of the silanols, aminopropyl functional amorphous polymer is formed with Si-O-Si bonds that results in a soft organosilica layer.[12] The organo-silica layer formed around the enzyme bears amine (-NH_3^+), hydroxyl

(-OH) and methyl (-CH_3) functional groups that provide concerted weak interactions, namely electrostatic, hydrogen bonding and hydrophobic interactions. The organosilica layer is PEGylated to ensure that there is no non-specific binding during recapture of the enzyme (discussed below).[13] The enzyme, which is bound to the surface of the AuNR through non-covalent interactions, is removed by exposure to sodium dodecyl sulfate (SDS). The removal of the enzyme results in cavities within the organosilica layer that are complementary in shape and chemical functionality to the enzymes. The polymer imprints are left to cure at room temperature to increase the porosity of the organosilica layer for an enhanced diffusion of the substrate molecules and to provide conformation flexibility to the enzyme critical for the catalytic activity.[12] Subsequently, the enzyme is recaptured by virtue of the molecular recognition of the imprints within the organosilica layer. In the final step, a thin organosilica capping layer is formed on the surface of the enzyme to complete the encapsulation process.

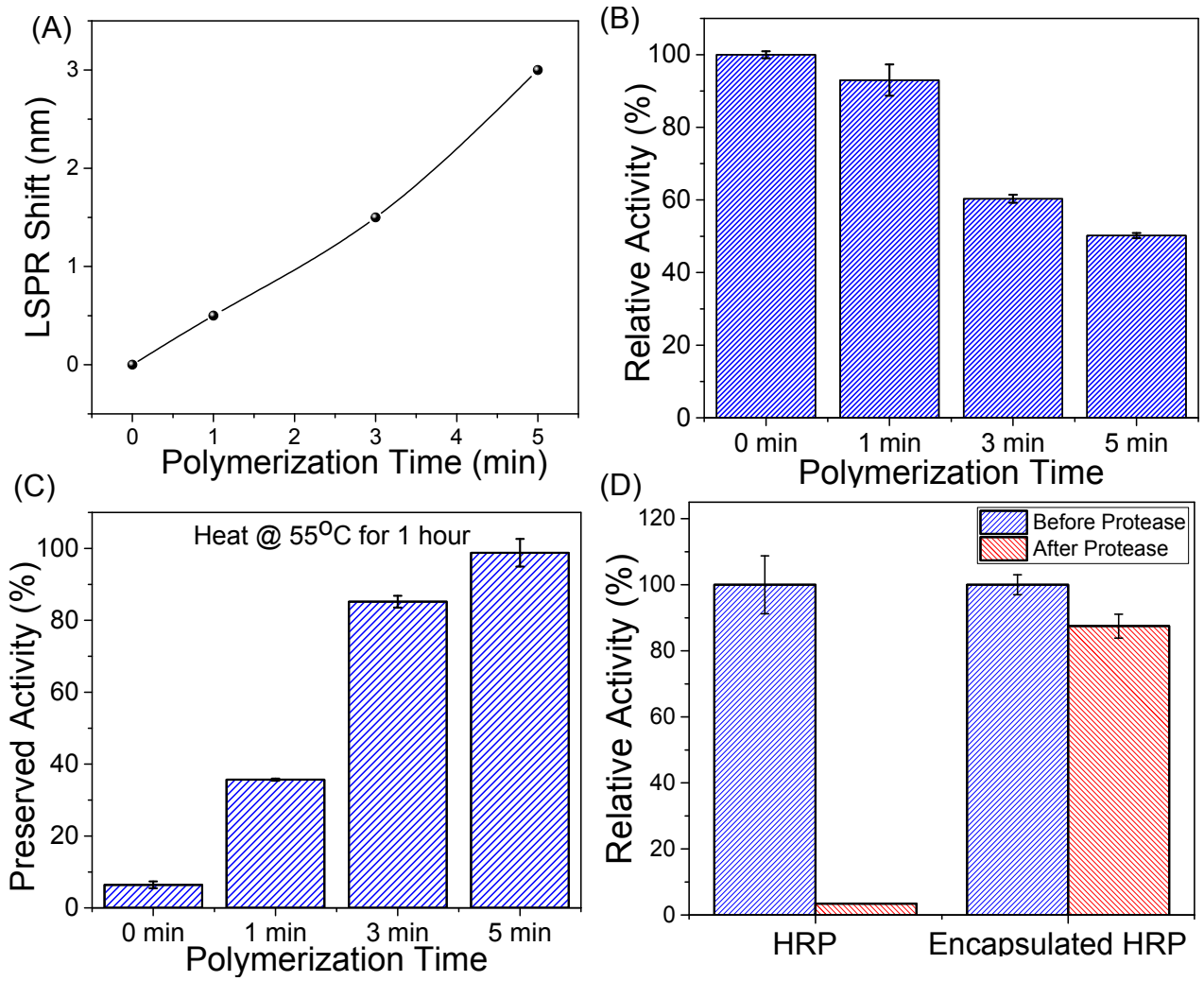

Figure 6: (A) LSPR wavelength shift upon the formation of capping layer on the recaptured enzyme after different polymerization times. (B) Relative activity of the polymer encapsulated enzyme after the formation of capping layer for different polymerization times. (C) Retained activity of the polymer

encapsulated enzyme after subjecting it to heat treatment at 55°C for 1 hour. (D) Retained activity of the polymer encapsulated enzyme after subjecting it to proteolytic degradation suggesting that the complete encapsulation prevents the protease access to the enzyme.

Each step in the polymer encapsulation procedure is monitored by the LSPR shift corresponding to the change in the refractive index around the plasmonic nanostructures. Extinction spectra of AuNR were obtained following each step in the encapsulation procedure: immobilization of AuNR-HRP conjugates on glass substrates (step 1), polymerization of the silane monomers (step 2), removal of the enzyme (step 3) and capture of the fresh enzyme (step 4) (Figure 5D). The LSPR wavelength of the AuNR exhibited a red shift (~8.5 nm) corresponding to the formation of an organosilica layer around the NR-HRP, a red-shift (~0.5 nm) due to the formation of a PEG layer and a blue shift (~5.5 nm) corresponding to the release of the enzyme. These steps are followed by rebinding of the enzyme (red shift of ~5.5 nm) and the formation of a capping layer (red shift of ~1.5 nm), which exhibit a progressive red shift due to the increase in the refractive index (Figure 5E). After the formation of the capping layer, the AFM image of the polymer encapsulated AuNR-HRP revealed an increase in the diameter of the bionanoconjugates after the organosilica encapsulation corresponding to the formation of the amorphous polymer layer (Figure 5F). Furthermore, the presence of organosilica layer on NR-HRP is confirmed by surface enhanced Raman scattering (SERS) spectroscopy (Figure 5G). In case of NR-HRP, a Raman band 1324 cm^{-1} was observed corresponding to the amide III vibrations of HRP.[11] After the formation of an organosilica layer, we noted Raman bands corresponding to Si-O-R stretching (1024 cm^{-1}), Si-O-Si stretching (1056 cm^{-1}), and $–CH_2$ bending (1205 cm^{-1} and 1234 cm^{-1}).[13]

As described above, the organosilica encapsulation is completed by the formation of a thin capping layer after rebinding the enzyme on the nanostructures. The thickness of the capping layer is controlled by the polymerization time during the final step. The LSPR shift corresponding to the formation of the capping layer increased with the polymerization time, indicating the increase in the thickness of the polymer layer (Figure 6A).[11] The increase in the polymer capping layer thickness resulted in a decrease in the relative enzyme activity due to the slower diffusion of the substrate through the polymer shell (Figure 6B). Despite the drop in the relative enzyme activity after the polymer capping layer, a significant improvement in the thermal stability and reusability is observed that underscores the importance of the capping layer (Figure 6C). We exposed the enzymes encapsulated with organosilica capping layer of varying thickness to 55°C for one hour. The preserved activity (retained activity after thermal or chemical treatment) increased with the increase in thickness of the capping layer. In the absence of capping layer, the preserved activity after thermal treatment was only 5% while the preserved activity in the case of five-minute polymerization capping layer was ~100%. This observation suggests that a thin organosilica capping layer after capture is essential to provide thermal stability to the polymer encapsulated enzyme. Note that both the bionanoconjugates and organosilica encapsulated bionanoconjugates were exposed to a single round of catalysis before measuring the thermal stability to remove the effect of loss in enzymes during catalysis, as discussed below.

We probed the biological stability of the organosilica stabilized enzyme by subjecting encapsulated and uncapped enzyme to proteolytic degradation. The activity of NR-HRP without organosilica shell reduced to ~5% while the polymer encapsulated enzyme retained ~90% of the

activity suggesting that the organosilica shell hinders the accessibility of the immobilized enzyme to protease providing excellent biological stability towards proteolytic digestion (Figure 4D). Thus, the polymer encapsulated enzyme can be used in harsh industrial settings and can be used independent of the storage condition.

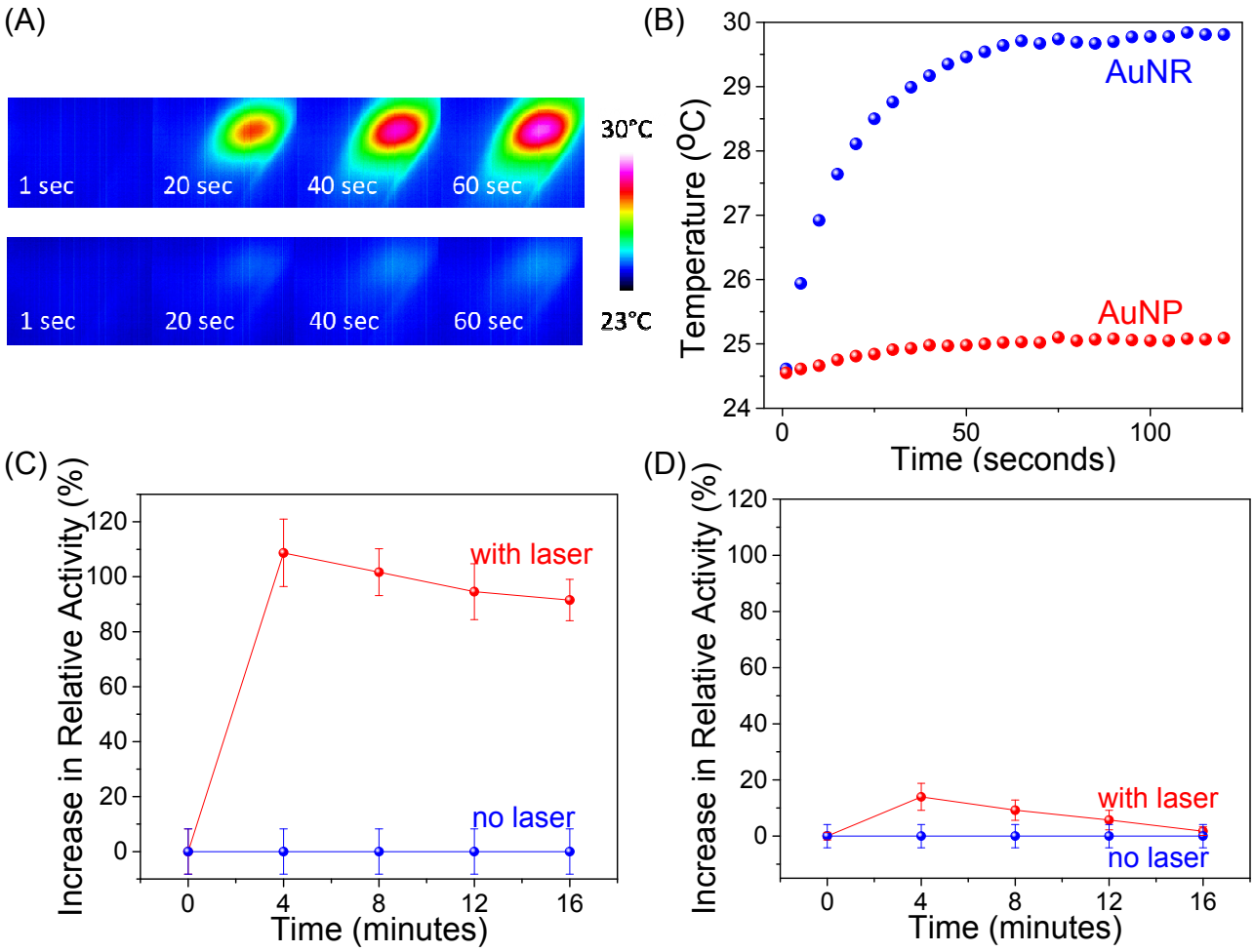

Figure 7: (A) IR images depicting the temperature rise of glass substrates adsorbed with (top) AuNR-HRP (on-resonance) and (bottom) AuNP-HRP (off-resonance) exposed to 808 nm laser. (B) Temperature profile in AuNR-HRP and AuNP-HRP as a function of laser irradiation time. Relative activity after different laser exposure times in (C) AuNR-HRP (on-resonance) and (D) AuNP-HRP (off-resonance).

The use of plasmonic nanostructures as enzyme supports provide the ability to use an external trigger to control and modulate the biocatalytic activity. Plasmonic nanostructures exhibit a large absorption cross-section and excellent photothermal ability (highly efficient light to heat conversion) enabling them to act as nanoscale heating elements.[14] To demonstrate externally-triggered modulation of bioactivity, we employed two different plasmonic nanostructures, namely, gold nanoparticles (AuNP) with an LSPR wavelength of 520 nm and AuNR with an LSPR wavelength of 800 nm. We compare the temperature rise of bioconjugated AuNRs (on-resonance) and AuNPs (off-resonance) upon exposure to

808 nm wavelength laser at a power of 400 mW/cm^2 (Figure 5A). We observed 5°C increase in temperature under laser illumination in the case of AuNR while the temperature in the case of AuNP did not exhibit a significant change over the entire duration of laser exposure (as measured by an IR camera) (Figure 7B). We studied the effect of laser exposure on the biocatalytic activity of organosilica encapsulated enzymes immobilized on the plasmonic nanostructures. We found that the activity of enzymes immobilized on AuNR increases by ~110% after 4 min laser exposure and retains the same activity for prolonged exposure (Figure 7C). However, in the case of AuNP-HRP, the activity increased by only 10% after 4 min laser exposure (Figure 7D). The increase in the biocatalytic activity can be correlated to the increase in temperature as observed from the IR images.

The increase in the biocatalytic activity in AuNR-HRP with laser irradiation and temperature rise is attributed to the increase in the fraction of the substrate molecules with an energy higher than the required activation energy for the successful collision with the enzyme. Additionally, an increase in the pore size of the organosilica polymer network due to the increase in the temperature results in an enhanced diffusion of the substrate molecules. In contrast, AuNR-HRP without polymer encapsulation showed a drop in the activity upon prolonged laser exposure unlike the polymer encapsulated AuNR-HRP, which is in agreement with previously reported results.[15] As a further confirmation, we exposed the polymer encapsulated enzymes to an elevated temperature of 30°C using an external source (heat oven) and found that the activity is enhanced by ~90%. The difference in the enhancements in the case of laser exposure and external heating can be attributed to the relatively higher local temperature on the surface of the AuNR in the case of laser exposure. Thus, the plasmonic nanostructures provide the ability to remotely control the activity of the polymer encapsulated enzyme to demonstrate an enhanced biocatalytic activity with light as an external trigger.

Metal-Organic Framework as Protective Coating for Functional Proteins

Functional proteins are highly susceptible to thermal denaturation, involving changes in secondary and tertiary structure and concomitant loss of function. Effective strategies for preserving the biofunctionality of such labile biomolecules is of utmost importance in a number of applications. For example, a wide range of conventional immunoassays and emerging biosensors rely on antibodies, which requires special handling and storage conditions, for example, transportation and storage within a “cold chain” system. Herein, we introduce zeolitic imidazolate framework-8 (ZIF-8), a metal-organic framework (MOF), as a simple and versatile protective material to preserve the antibody recognition capability of biochips under ambient and elevated temperatures. A plasmonic nanobiosensor is employed as a transduction platform for monitoring the formation and removal of the protective MOF coating and to quantify the biopreservation ability of MOF under various extreme storage conditions. Formation of the protective MOF coating is facile, and a simple water rinsing step can restore the biofunctionality of the MOF-coated biochip, thereby making it highly convenient for use in point-of-care and resource-limited settings. To the best of our knowledge, this is the first report using MOF as the material to preserve the biofunctionality of antibody (in its surface-bound state). We believe this energy-efficient and environmentally-friendly approach eliminates the needs for cold chain and temperature-controlled storage/shipping of diagnostic reagents and materials, thereby extending the capability of antibody-based biosensors to various resource-limited environments. More broadly, the

MOFs are expected to play a powerful role in the realization of ultrastable biodiagnostics and therapeutics.

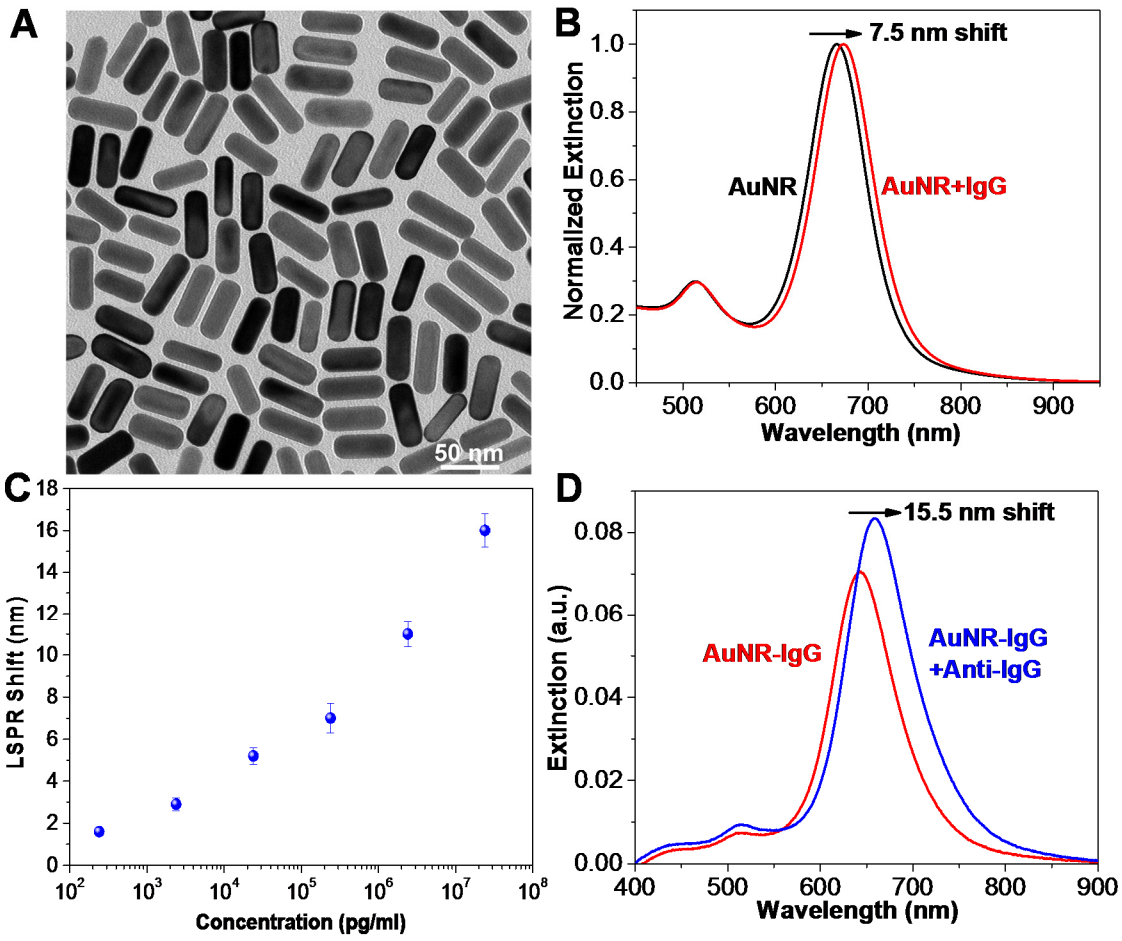

Figure 8. (A) TEM image of AuNRs used as plasmonic nanotransducers. The dimension of the AuNRs is 48×18 nm. (B) Extinction spectra showing the LSPR shift after conjugation of AuNR with IgG in solution. The λ_{max} red shifts by 7.5 nm. (C) LSPR shift of AuNR-IgG on glass substrate upon exposure to various concentrations of anti-IgG solutions showing the monotonic increase in LSPR shift with concentration. Error bars represent standard deviations from three different samples. (D) Extinction spectra of AuNR-IgG conjugates on the glass substrate before and after exposure to anti-IgG (24 μg/ml). The λ_{max} red shifts by 15.5 nm.

Rabbit IgG and goat anti-Rabbit IgG (termed IgG and anti-IgG henceforth) were employed as model antibody and bioanalyte, respectively, to establish the proof-of-concept. Here, gold nanorods (AuNRs) were used as plasmonic nanotransducers for label-free sensing because of their large refractive index sensitivity and excellent tunability of the LSPR wavelength.[20] We synthesized AuNRs with a length of 48.2±1.8 nm and a diameter of 18.2±1.1 nm using a seed-mediated approach (Figure 8A).[21] As described earlier,[20] the conjugation of the antibody (IgG) to AuNRs is achieved by conjugating IgG molecules to a bifunctional polyethylene glycol (COOH-PEG-SH) chain and

subsequently attaching the formed IgG-PEG-SH onto AuNRs surface through gold-thiol linkage. The PEG chain acts as a flexible spacer, increases the accessibility of target biomolecules to IgG and also serves as a stable protective layer around AuNRs to minimize non-specific binding. After conjugating IgG onto AuNRs surface, the longitudinal LSPR wavelength of the AuNRs showed a 7.5 nm red shift due to the increase in the refractive index of the medium surrounding the AuNR (Figure 8B). These AuNR-IgG conjugates were then immobilized onto the 3-mercaptopropyl-trimethoxysilane-functionalized glass surfaces. To probe the sensing capability of the plasmonic nanobiosensor, the substrates were exposed to different concentrations of anti-IgG leading to its specific binding to IgG, which can be quantified by the red-shift in the LSPR wavelength of AuNRs. We observed a monotonic increase in the LSPR shift with an increasing concentration of the anti-IgG. The limit of detection was found to be 240 pg/ml (Figure 8C), consistent with our previous reports.[19] Considering that the LSPR wavelength red shifted maximally by 15.5 nm at the highest concentration (24 μg/ml) of anti-IgG (Figure 8D), in the following experiments we have employed 24 μg/ml of anti-IgG to quantify the biorecognition capability of antibody (IgG) subjected to different storage conditions.

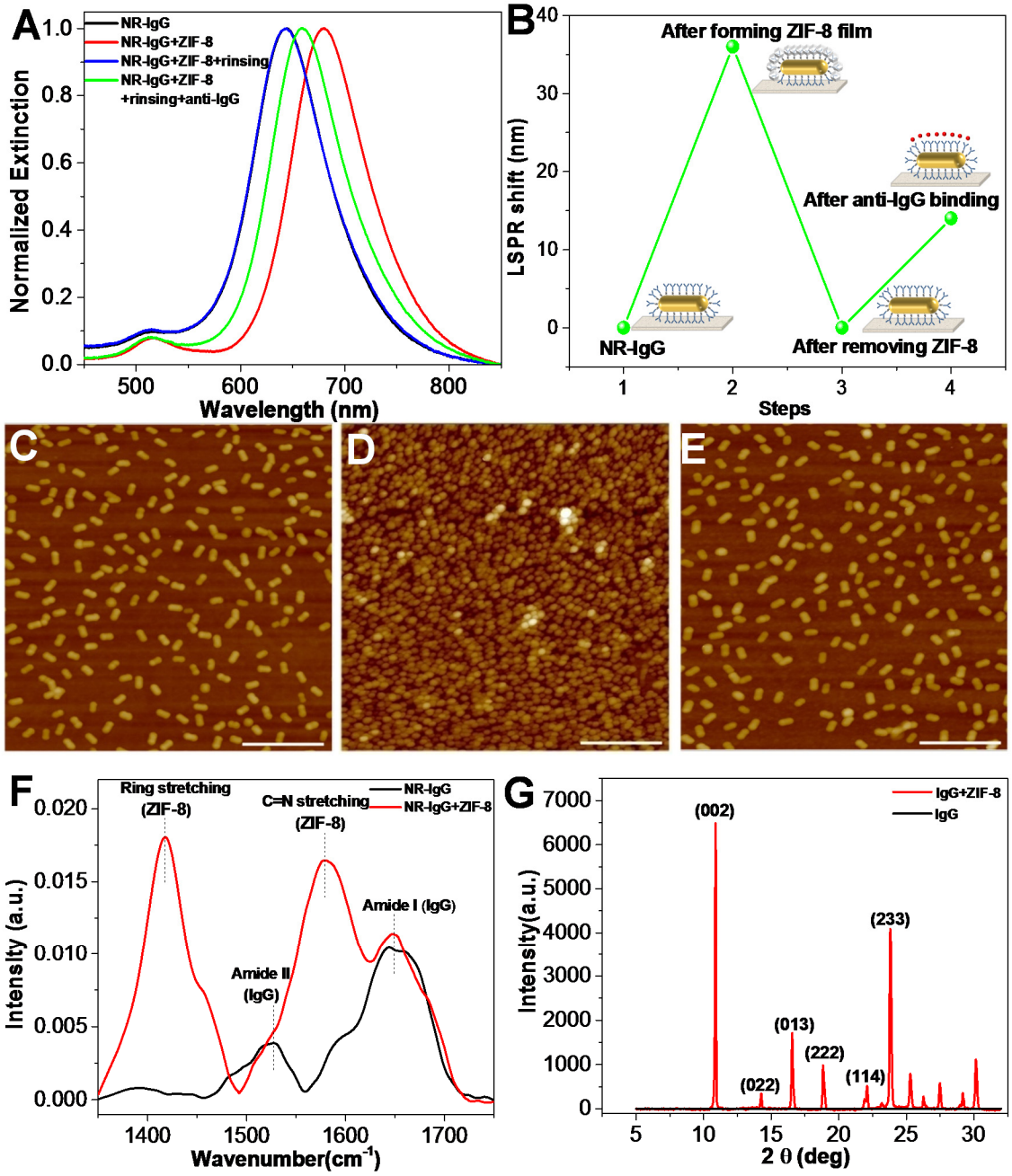

Figure 9. (A) Extinction spectra of AuNR-IgG conjugates on the glass substrate before (black) and after ZIF-8 film coating (red), after removing ZIF-8 film (blue) and after exposure to 24 μg/ml of anti-IgG (green). (B) LSPR shift corresponding to each step shown in (A). AFM images showing (C) uniformly adsorbed AuNR-IgG on glass substrate before ZIF-8 film coating (D) AuNR-IgG conjugates covered by ZIF-8 film (E) complete removal of ZIF-8 after rinsing with distilled water at pH6. Scale bars: 500 nm. (E) FTIR spectra of AuNR-IgG before and after ZIF-8 coating. (F) XRD spectra of AuNR-IgG before and after ZIF-8 coating.

MOF has been previously used in encapsulating an enzyme and providing thermal stability.[22] The preservation mechanism is attributed to the small pore size of MOF and coordination interactions between the carbonyl groups of the protein backbone and the Zn cations of ZIF-8, providing proteins with tight encapsulation.[15, 23] In this study, we posit that a MOF coating on a biosensor surface would protect the biorecognition capability of the underlying antibody. In addition to the detection and quantification of target analytes, refractive index sensitivity of LSPR wavelength of AuNRs can also be exploited to monitor the formation and removal of the MOF coating (Figure 9A and 9B). After immersing the biochips with immobilized AuNR-IgG into MOF precursor solution (mixture of 2-methylimidazole and zinc acetate) for 3 hours, the LSPR wavelength exhibited a ~30 nm red shift (step 2 in Figure 9B), suggesting the formation of MOF coating on top of the AuNR-IgG conjugates. Interestingly, immersing the bare AuNRs-immobilized glass substrate into MOF precursor solution for 3 hours resulted in a LSPR wavelength shift of only ~ 2 nm possibly due to the adsorption of MOF precursors on AuNR or extremely slow growth of ZIF-8 on bare AuNR. This is in stark contrast with the rapid growth if ZIF-8 on bioconjugated nanostructures.[16] After storing the MOF-coated plasmonic biochips at desired temperature and duration, the MOF protective coating can be quickly removed by rinsing the biochip with distilled water at pH6. The complete removal of the MOF is evidenced by a ~30 nm blue shift in the LSPR wavelength (step 3 in Figure 9B). It is important to ensure complete removal of the MOF protective coating and restoration of the biorecognition capability of the biosensor before exposing the plasmonic biochips to the analyte solution. Subsequently (step 4 in Figure 9B), the restored biochip displayed a 14 nm red shift upon specific binding of anti-IgG (24 μg/mL) to IgG. The percentage of retained recognition capability (%) was used to quantitatively evaluate the antibody preservation efficacy of MOF under various storage conditions. The retained recognition capability was calculated as the percentage of the red shift upon specific binding of anti-IgG (24 μg/mL) to IgG on a restored biochip after several days of storage at elevated temperatures compared to the red shift obtained from the same batch of freshly-made substrate (which was considered as the reference sample tested instantly without MOF coating). For example, the red shift of 14 nm compared to the red shift of 16 nm in the case of the reference sample in the same batch corresponds to a retained recognition capability of 87.5% (Figure 9A and 9B). Therefore, ~88% recognition capability of the antibody-based biochip was found to be preserved after two days of storage at room temperature.

The MOF film formation and removal were further confirmed by atomic force microscope (AFM) imaging. Prior to incubating the substrate with MOF precursor solution, the AuNR-IgG conjugates were found to be uniformly distributed on the substrate (Figure 9C). After coating process, the AuNR-IgG conjugates were found to be covered by the MOF film that exhibited dense grainy morphology (Figure 9D). This is further confirmed by the scanning electron microscope (SEM) images. After rinsing the substrate with water at pH 6, the AuNR-IgG conjugates were exposed without any MOF residue on the substrate (Figure 9E). The AFM scratch test indicated the thickness of the MOF film to be ~50 nm, which is sufficient to completely cover AuNR-IgG conjugates (~22 nm height). To ascertain that ZIF-8 crystals were formed on the surface of AuNR-IgG conjugates, Fourier transform infrared spectroscopy (FTIR) and X-ray diffraction (XRD) were employed (Figure 9F and 9G). FTIR spectrum (black) obtained before the formation of the MOF layer exhibited absorption peaks at 1640-1650 cm^{-1} and 1520-1530 cm^{-1}, corresponding to amide I and amide II bands of IgG, respectively. After the MOF formation, the FTIR spectrum exhibited new absorption bands corresponding to MOF apart from the

amide I and amide II bands of the protein. The characteristic absorption peak at 1583 cm^{-1} corresponds to the C=N stretching of imidazole and the peak at 1420 cm^{-1} is associated with the imidazole ring stretching.[24] These characteristic absorption bands were also observed in the FTIR spectrum obtained from pure ZIF-8. Interestingly, the amide I vibrational mode for the MOF-coated AuNR-IgG shifted to higher frequency (from 1643 to 1649 cm^{-1}), suggesting the protein–MOF interaction due to the coordination between the Zn cations and the carbonyl group of the proteins.[15] Furthermore, XRD measurements confirmed the formation of ZIF-8 crystals on the top of AuNR-IgG surface (Figure 9G). The XRD patterns and related peak positions were in agreement with typical structure of ZIF-8[25] except for the absence of (011) and (112) plane, implying the possible orientation of ZIF-8 formed on AuNR-IgG immobilized substrate. The XRD pattern also shows a strong peak at 10.88°, indicating the partial orientation of the crystals in (001) direction. It has been previously reported that the surface properties can significantly influence the nucleation and crystal growth of ZIF-8.[26] This suggestion was further confirmed by powder XRD of pure ZIF-8 and ZIF-8 formed in IgG solution, which exhibited all peaks of ZIF-8 including those corresponding to (011) and (112) planes and relatively low intensity peak at 10.88°.

Before performing a comprehensive investigation of the efficacy of the ZIF-8 layer as protective coating for preserving the antibody recognition capabilities, it is important to determine whether the preservation process itself would compromise the biochip performance. An important aspect that needs to be considered is the effect of ZIF-8 growth and rinsing on the recognition capability of the antibodies conjugated to the plasmonic nanostructures. To address this aspect, we coated the ZIF-8 film onto a freshly-made AuNR-IgG immobilized biochip and immediately removed the ZIF-8 film. After incubation of the biochip with the analyte solution containing 24 μg/mL of anti-IgG, we observed a ~16 nm red shift, very close to that noted for the reference sample. The virtually complete preservation of the specific recognition capability of IgG-AuNR conjugates after subjecting the biochip to the preservation process (i.e., MOF layer growth and removal) indicates that the MOF-based preservation steps do not adversely affect the biochip performance.

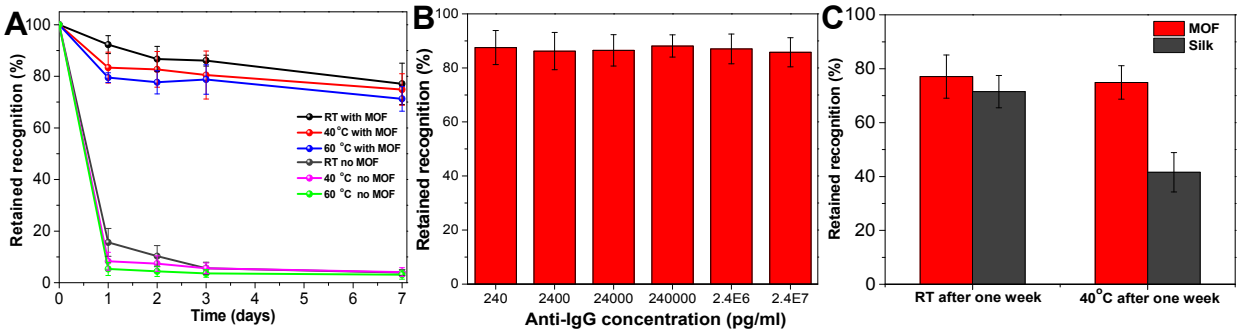

Figure 10. (A) Retained recognition capability of MOF-coated IgG-AuNR conjugates on glass substrates stored at room temperature, 40 °C and 60 °C for different durations. (B) Retained recognition capability of MOF-coated IgG-AuNR conjugates stored at room temperature for three days measured by exposing the substrates to different concentrations of anti-IgG. (C) The comparison of preservation efficiency between MOF and silk as the protective materials after one week at room temperature and 40 °C. Error bars represent standard deviations from three independent samples.

Next, we set out to investigate the efficacy of MOF to preserve the biorecognition ability of IgG conjugated to AuNR upon exposure to harsh conditions (such as high temperatures) that would normally lead to denaturation and loss of recognition capabilities. The plasmonic biochip with and without MOF coating were stored at room temperature, 40°C and 60°C for one week. To eliminate the influence of relative humidity variations in the standard laboratory environment, all the samples were stored in sealed containers. ZIF-8 has excellent thermal stability (up to 550 °C), as well as chemical resistance to boiling alkaline water and organic solvents.[27] However, it is not stable in acidic environment because of the loss of the coordination between the zinc ions and imidazolate at pH 5.0–6.0.[28] Therefore, as long as ZIF-8 protected surfaces are stored in dry or non-acidic conditions, the ZIF-8 shell should be stable. For the same reason, water at pH6 was employed to completely remove the ZIF-8 protective layer and restore the bio-functionality of antibodies conjugated to nanotransducers. Different substrates were sampled at selected time intervals (1, 2, 3, and 7 days) to monitor the changes in the biorecognition capability of the antibodies (Figure 10A). Samples with MOF coatings showed only a ~20% loss in biorecognition capability after storage at room temperature (25 °C) for one week compared to the nearly complete loss in biorecognition capability for substrates without MOF protective layer. Even at higher temperatures, 40 °C and 60 °C, MOF-coated biochips retained over 70% of biorecognition ability after one week. In contrast, substrates without an MOF protective layer lost over 90% of biorecognition capability within the first day at 40 °C and 60 °C. Furthermore, we selected one storage condition (three days storage at room temperature) and investigated the detection sensitivity (LSPR shift) at varying concentrations of anti-IgG after removal of ZIF-8. The LSPR shifts at different concentrations of anti-IgG were compared with the results from freshly-made samples (the results in Figure 8C). Across the entire concentration range tested here, we noted a consistent ~15 % decrease in LSPR shift (Figure 10B). The limit of detection of the plasmonic biosensor stored for three days at room temperature is found to be 240 pg/ml (defining 1 nm as 3σ noise level), which is similar to a freshly prepared biosensor. Compared to our previous approach involving silk fibroin as a protective layer, MOF coating is vastly superior in terms of biopreservation efficacy, ease of formation and removal, as well as availability and cost of the raw materials.[19] While the silk-coated plasmonic biochips retained a biorecognition capability of ~40% after one week at 40 °C, the MOF-coated biochips retained over 70% of biorecognition ability under identical storage conditions (Figure 10C). Furthermore, complete removal of silk film can be difficult if the silk-encapsulated biochips are subjected to harsh conditions such as high temperature or organic solvents, which results in the conversion of silk I to insoluble silk II state.[29] In addition, both 2-methylimidazole and zinc acetate are commercially available, whereas silk fibroin extraction and purification procedures involve several processing steps that need to be executed with significant caution. Taken together, MOFs are a better choice compared to silk fibroin as the protective layer to stabilize antibody-based biosensors against extreme environments.

Adsorption behavior of silk fibroin on amphiphilic graphene oxide

In a related effort, we have studied the charge-dependent adsorption behavior of silk fibroin, a multi-domain protein, on amphiphilic graphene oxide (GO) under various pH conditions. GO-silk composites have gained a significant interest in the recent times because of the unique mechanical properties of both GO and silk and their ability to form layered structures that exhibit a striking resemblance to the layered (brick-mortar) composites found in nature. However, various aspects of the interaction between

silk and graphene oxide (e.g., conformation and distribution of the silk chains on chemically heterogeneous GO surface) are not completely understood. In this study, we demonstrate that the interaction between the silk fibroin chains and GO can be modulated by altering the pH of the silk fibroin solution. We employed atomic force microscopy (AFM) and Fourier transform infrared (FTIR) spectroscopy to probe the distribution and the secondary structure of silk fibroin adsorbed on GO.

Considering the multi-domain structure and amphiphilic nature of silk fibroin, adsorption of silk chains on a surface can occur through hydrogen bonding, electrostatic or hydrophobic π-π interactions depending on the chemical functionality of the surface and the specific domains of the silk fibroin interacting with the surface.[16] Due to the amphiphilic nature of GO, the interactions between silk fibroin and GO can be polar or hydrophobic depending on the ionization state of the silk chains. At pH 4, we observed a very high density of silk chains adsorbed on the surface of GO due to polar and hydrophobic interactions (Figure 11A, E). The close to zero zeta potential of the silk at pH 4 also results in intermolecular attractions between the silk chains through hydrophobic and van der Waals interactions. Hence, most of the molecular clusters of silk are possibly comprised of more than one chain of silk fibroin. As the pH is increased, the amount of silk on the GO reduces due to which the distance between the silk globules increases. At pH 7, due to the negatively charged state of the silk (zeta potential of -14 ± 2 mV), electrostatic repulsion between the silk and GO dominates the adsorption process (Figure 11D, H). The electrostatic repulsion between the silk chains and oxidized domains of GO forces the adsorption of silk on the unoxidized hydrophobic domains of GO through hydrophobic interactions. The adsorption of silk on GO is also influenced by the intermolecular electrostatic repulsions between the silk chains resulting in an increased intermolecular separation. The average distance between the silk globules is higher at high pH due to the intermolecular electrostatic repulsions of the negatively charged silk at pH 7 (Figure 11(A-H)).

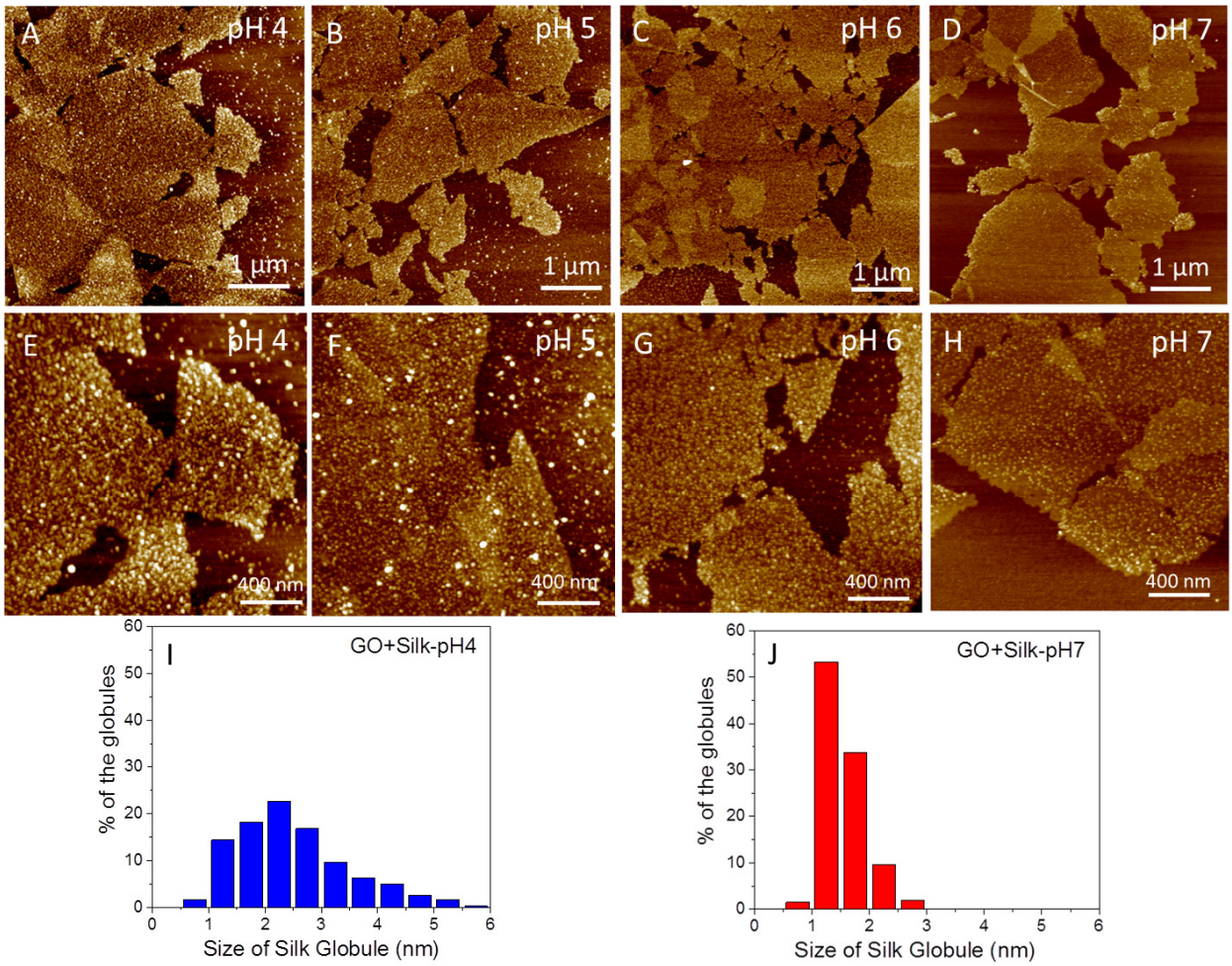

Figure 11: AFM images of silk fibroin adsorbed on GO flakes at (A,E) pH 4 (B,F) pH 5 (C,G) pH 6 (D,H) pH 7. Z-scale: 10 nm. The size of the globules of silk adsorbed on GO varies as a function of the pH of silk solution. Histograms showing the globule size distribution of silk fibroin adsorbed on GO at (I) pH 4 and (J) pH 7.

The dimensions of the silk clusters provide an additional insight into the conformation of the silk fibroin adsorbed on GO. At pH 4, the size of the molecular cluster exhibits a broad distribution with a peak at ~2.5 nm (Figure 11 I). The broad distribution in the size of silk adsorbed on GO at pH 4 can be attributed to the heterogeneous adsorption (on both hydrophilic and hydrophobic domains of GO) resulting in a broad spectrum of site-dependent conformations and intermolecular interactions. Under this pH condition, silk chains interact with the GO surface via both polar and hydrophobic interactions. The size distribution of the globules indicated the formation of molecular clusters of silk with some layering associated within the secondary structure.[17] At pH4, considering that the zeta potential of the silk is close to zero, there is very little electrostatic repulsion between the silk chains causing the compact globules to form molecular clusters on the surface through hydrophobic and polar interactions. On the other hand, at pH 7, the silk chains exhibited a narrow height distribution with a peak at ~1.3 nm (Figure 11J). Significantly, the globule size of the silk chains on the GO surface at pH 7 is significantly lower compared to the clusters observed at pH 4. The repulsive interactions of the charged moieties on

the silk chain at pH 7, resist the formation of clusters, causing the chains to adapt a pancake-like conformation. The narrow distribution of the silk chains on the GO at pH 7 compared to pH 4 can be attributed to homogeneity of the interfacial interactions between GO and silk, which is predominantly hydrophobic in nature. The hydrophobic blocks of the silk acting as trains closely interact with the hydrophobic domains of GO surface while the hydrophilic linkers (acting as loops and tails) interact with the solvent creating a pan-cake conformation of the silk on GO surface.

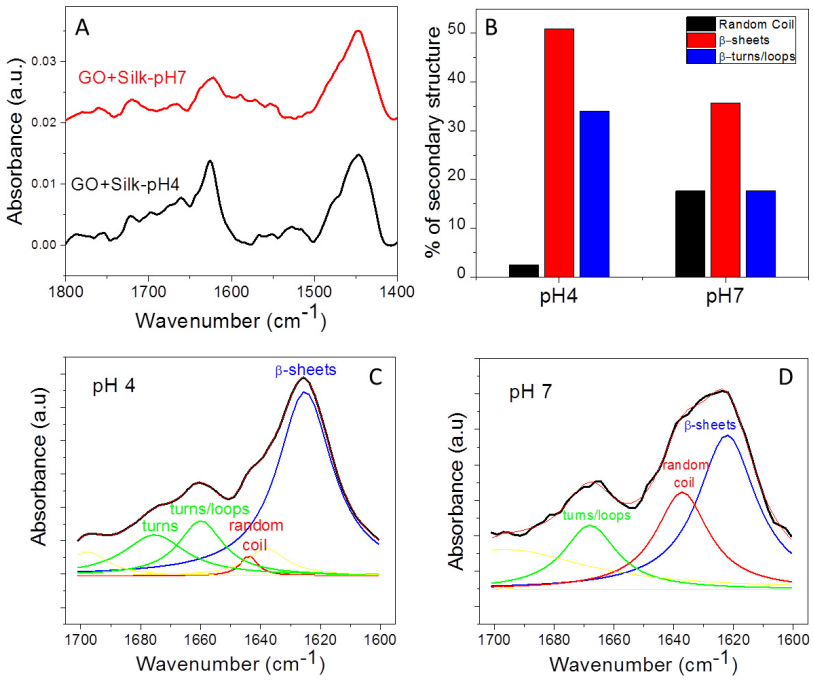

Figure 12: (A) FTIR spectra of silk fibroin adsorbed on GO at different pH indicated in the plot. (B) The percentage of different conformations of silk adsorbed on GO at different pH. Plots showing the amide peak deconvolution using Lorentzian peaks to estimate the relative amounts of different conformations of silk on GO at (C) pH 4 (D) pH 7

To probe the secondary structure of the silk adsorbed on GO at different pH values, we employed FTIR spectroscopy. Amide I (1700-1600 cm^{-1}) and amide II (1600-1500 cm^{-1}) bands of the infrared absorption spectra corresponding to the peptide backbones, provide an insight into the secondary structure of the silk fibroin.[18] The absorption bands of random coil are noted to be at 1640-1654 cm^{-1} (amide I) and 1535-1545 cm^{-1} (amide II) whereas the bands at 1610-1630 cm^{-1} (amide I) and 1510-1520 cm^{-1} (amide II) are assigned to β-sheets. [19,20,21] The FTIR spectra obtained from the silk adsorbed on GO at different pH values are shown in Figure 12A. The conformation of the silk on the surface of GO at different pH values is assessed by deconvoluting the amide I band to determine the fraction of different secondary structures of the silk fibroin chains.[22] The peak deconvolution used a Lorentzian band shape with an optimal resolution enhancement factor depending on the quality of the data. The number of components of the deconvoluted peaks was determined based on the quality of the fit and reproducibility of the peak positions. After deconvoluting the amide I peaks at 1700-1600 cm^{-1}, the deconvoluted peak at 1623 cm^{-1} represents the amount of β-sheet content whereas the peak

at 1645 cm^{-1} represents the amount of random coil conformation[23] of the adsorbed silk at different pH conditions. (Figure 12C and 12D).

Figure 12B shows the relative percentages of various secondary structures (β-sheets, turns/loops and random coil) calculated from deconvoluting the amide I and amide II regions of the FTIR spectra. The amount of β-sheet content in silk adsorbed on GO at pH 4 is found to be ~50%, which agrees with a previous report.[24] This can be attributed to the polar interactions between silk chains and the substrate, which reduce the stability and content of random coil conformation.[25-26] Further, the amount of β-sheet content of silk adsorbed on GO at pH 7 reduced to ~35% suggesting that the silk globules that bind on the surface of GO through hydrophobic interactions induce a random coil conformation due to the feasibility of the silk interacting through hydrophobic domains. As a result, the amount of silk in random coil conformation increased to ~18% at pH 7 reducing the net β-sheet, β-turn and loop conformations. A similar behavior was reported in the past in silk-like peptides upon binding to a hydrophobic surface.[27]

To conclude the adsorption behavior of silk on amphiphilic GO is found to be highly pH-dependent. In acidic pH conditions (*i.e.* pH<pI), a high density of silk chains were found to adsorb on the GO surface, whereas an increase in pH resulted in a progressive decrease in the density of the adsorbed silk chains. This pH-dependent adsorption is ascribed to the electrostatic interactions between the negatively charged GO surface and the tunable ionization of the silk molecules. The secondary structure of silk fibroin chains adsorbed on GO was also found to be highly dependent on the pH. This study provides a deeper understanding of the interaction between GO and silk fibroin that is critical for the design and fabrication of bioinspired nanocomposites with tailored mechanical properties.

Functional biofoams based on bacterial nanocellulose

We have demonstrated plasmonic biofoams from various biomaterials, such as bacterial nanocellulose (BNC) and regenerated silk fibroin (Figure 13A). BNC of desired thickness (1-5 mm) is obtained from a static culture of *Gluconacetobacter hansenii* grown under aerobic condition at room temperature (see Methods for details).[28-30] BNC-based aerogels are attractive due to their inherent three-dimensional nanofibrous structure, excellent mechanical flexibility (unlike conventional brittle silica aerogels), high purity, rich surface functionality, and cost-efficiency, scalable and environment-friendly synthesis.[28, 31-34] The *as synthesized* BNC is harvested and processed to obtain nanocellulose hydrogel with an extremely high water content (~99% by weight). Subsequently, the hydrogel is freeze-dried to obtain BNC aerogel with ~98% porosity, ultralow density (~20 kg m^{-3}) and extremely large specific surface area (~75 m^2 g^{-1}). Freeze-dried BNC aerogel is comprised of a highly open microporous non-woven 3D network of cellulose nanofibrils (diameter of 20-100 nm) (Figure 13B). Considering that bacteria form the cellulose fibers at the air/liquid interface, the cellulose nanofibrils are preferentially oriented parallel to the surface (i.e. normal to the thickness) of the aerogel structure, which results in denser physical entanglements of the cellulose nanofibrils parallel to the surface compared to that along the

thickness.[28, 32] A representative cross-section SEM image of the BNC aerogel reveal a dense layers of cellulose fibers separated by a layer of sparse “tie” fibers resulting in a layered structure (Figure 13B).

We employ gold nanorods (AuNRs) of ~52 nm in length and ~13 nm in diameter as plasmonic nanostructures for the fabrication of plasmonic biofoams, owing to their tunable longitudinal LSPR wavelength and large electromagnetic field enhancement at sharp ends.[11, 35-36] To obtain a uniform and high density adsorption of AuNRs on BNC, we immersed BNC aerogel into a highly concentrated solution of AuNRs (2 μM) for 12 hours, followed by thorough rinsing with water to remove weakly bound nanostructures. The adsorption is facilitated by a capillary force-driven uptake of AuNRs and non-covalent interactions (electrostatic and van der Waals interactions) between positively charged AuNRs and hydroxyl groups of cellulose nanofibers. Following the adsorption of AuNRs on cellulose nanofibers, BNC is freeze-dried to result in a plasmonic aerogel, which exhibited a deep green color in contrast to the white color of the pristine BNC aerogel (Figure 13A). The SEM images of the plasmonic aerogel revealed a highly dense and uniform adsorption of AuNRs on the cellulose nanofibers (Figure 5C, D). Cross-section SEM images of the plasmonic aerogel depict the highly open porous structure, which ensures the accessibility of the plasmonic nanostructures. The extinction spectra from AuNR solution and plasmonic aerogel exhibit two distinct bands corresponding to the transverse (low wavelength) and longitudinal (high wavelength) LSPR (Figure 13E). The longitudinal plasmon band of the plasmonic aerogel, which is highly sensitive to the aspect ratio and assembly/aggregation of the nanostructures, indicates the well-preserved optical properties of the nanostructures with no indication of aggregation. The extinction spectra from plasmonic aerogel revealed a blue shift of ~110 nm in the longitudinal LSPR band compared to that of AuNR solution, due to the decrease in the effective refractive index of surrounding medium (from water to air+cellulose nanofiber).

Significantly, the immersion-assisted adsorption and freeze-drying process described here preserves the size, shape, and optical properties of plasmonic nanostructures incorporated into the aerogel, an important factor that determines the functional attributes of the aerogels. The AuNRs content in the plasmonic aerogel was measured to be ~57 wt% by thermogravimetric analysis (TGA), which can be varied by controlling the concentration of AuNRs solution and the incubation time. The number density of AuNRs in the aerogel is calculated to be ~10^{15} cm^{-3}, which corresponds to a high concentration of AuNRs ~1.5 μM in the aqueous solution and surface coverage percentage of ~48% on cellulose nanofibrils. Considering the complete preservation of the structure and properties of the nanostructures, plasmonic aerogel can be essentially treated as a “frozen” solution of plasmonic nanostructures with an extremely high concentration, yet providing virtually uninhibited access to the AuNR surface.

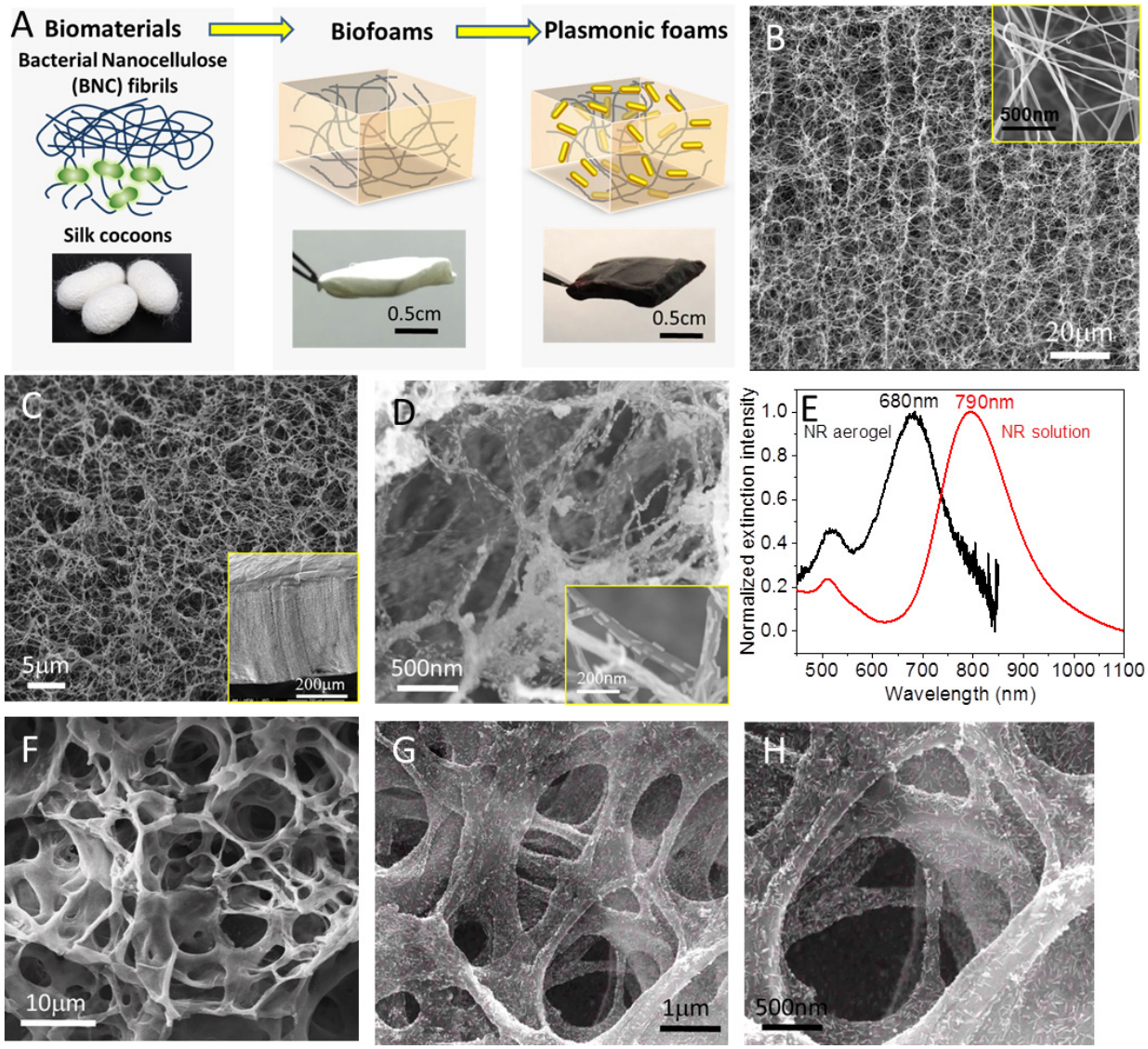

Figure 13. Plasmonic biofoams based on bacterial nanocellulose or reconstituted silkworm silk (A) Schematic illustration showing the fabrication of plasmonic foams (Two photographs in bottom right show the aerogel before and after dense loading of gold nanorods (AuNRs)). SEM images of (B) cross-section of BNC aerogel showing non-woven 3D network of cellulose nanofibrils with a highly open microporous structure (Inset: corresponding high magnification SEM image showing individual nanofibers), (C) cross-section of plasmonic aerogel depicting the preserved highly open porous structure, which ensures the accessibility of the plasmonic nanostructures and (D) corresponding high resolution image of plasmonic aerogel cross-section revealing dense and uniform adsorption of AuNRs on the nanofibers of the aerogel (Inset shows individual fibers decorated with AuNRs) (E) Extinction spectra of AuNRs solution and plasmonic aerogel indicating the well-preserved ensemble optical properties of the nanostructures with no indication of aggregation, in which two distinct bands

corresponding to the transverse (low wavelength) and longitudinal (high wavelength) LSPR. SEM images of silk-based plasmonic aerogels showing (F) microcellular morphology with open porous structure and (G, H) corresponding higher magnification images showing the uniform adsorption of AuNRs on silk surface.

We demonstrated that plasmonic biofoam is a versatile optically-active platform that can be harnessed for numerous applications including (i) an ultrasensitive chemical detection using surface enhanced Raman scattering (SERS); (ii) a highly efficient energy harvesting and steam generation through plasmonic photothermal heating; and (iii) optical control of enzymatic activity by triggered release of biomolecules encapsulated within the aerogel. Our results demonstrate that 3D plasmonic biofoam exhibits a significantly higher sensing, photothermal, and loading efficiency compared to conventional 2D counterparts. The design principles and processing methodology of plasmonic aerogels demonstrated here can be broadly applied in the fabrication of other functional foams. In contrast to conventional 2D plasmonic surfaces, the plasmonic biofoam demonstrated here offers plasmonically-active 3D space that can support a broad range of applications including sensing, actuation, energy harvesting, catalysis and triggered release. The approach demonstrated can be easily extended to other organic, inorganic and hybrid nanomaterials to realize functional 3D materials with well-preserved nanoscale structure and properties.

Elastoplastic deformation of silk micro- and nanostructures

We demonstrated the fabrication of low-dimensional patterned silk films and silk micro/nanopillars and their transfer to stretchable substrates. The silk micro- and nanostructures exhibited extremely high ductility with large local deformation (up to ~230% local strain) and the extent of local deformation before failure was found to be secondary structure-dependent. The successful transfer of the patterned silk films to stretchable substrates without the use of any organic solvent enabled us to probe the changes in the secondary structure of silk micro- and nanostructures upon mechanical deformation.

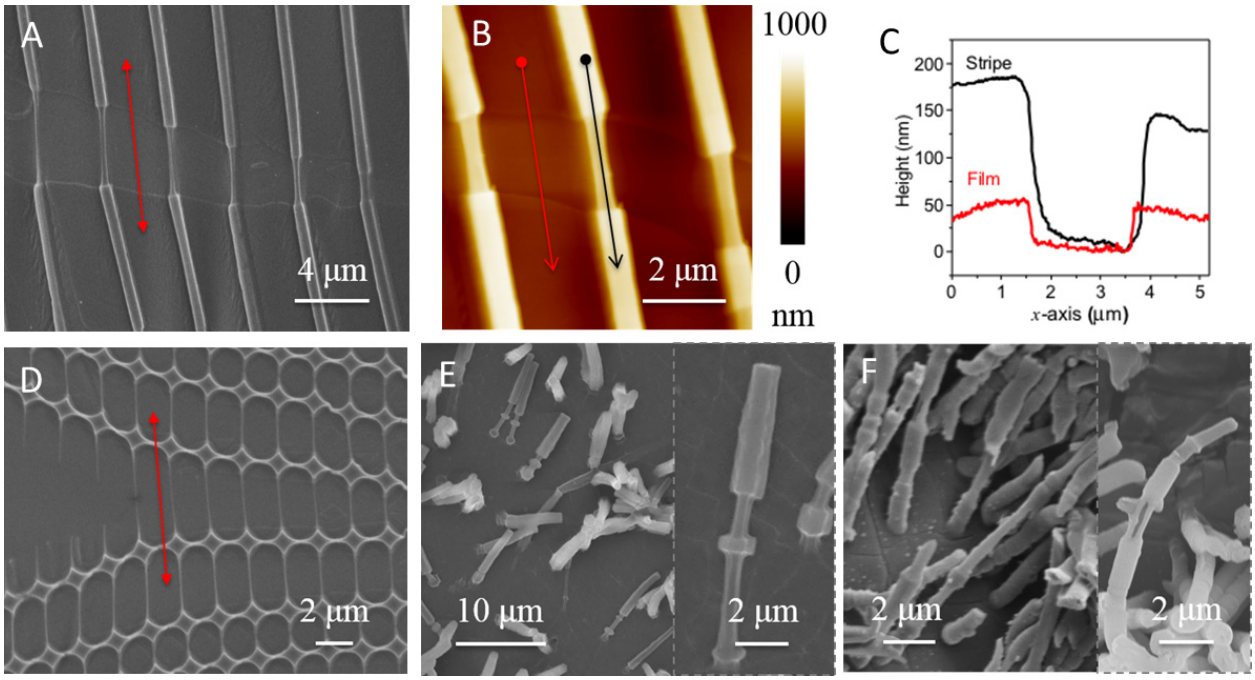

Figure 14: (A) SEM image of stretched silk film with stripe pattern. (B) AFM height image of stretched stripe patterned silk film. (C) Height profile along the indicated arrows in (b). SEM image of (D) stretched grid patterned silk film, (E) deformed silk micropillars and (F) deformed silk nanotubes.

To investigate the mechanical behavior of patterned silk films, soft PDMS substrates were stretched uniaxially to induce a deformation in the silk film. The stripes on silk films clearly showed necking-like behavior under stretching (Figure 14A). Although necking was also observed in the continuous silk film below the stripes (surface relief structures), the silk stripes made the neck-like local deformation clearly visible (Figure 14B, C). Local extension ratio was calculated from the stretched grid patterned silk films, which revealed a local ultimate strain of 230% (Figure 14D). The ductile or elastoplastic behavior of patterned silk films was further studied in silk micro/nanopillars by stretching 1D micro- and nanostructures using a solid adhesive by gentle contact followed by slow peeling. This tape peeling test results in a complex interplay of forces, revealing the mechanical response of silk structures in a wide variety of deformational modes. While the initial contact with the adhesive tape results in an axial and radial compression of the micro/nanostructures, the peel off process results in a complex tensile and shear deformation in the 1D nanostructures. A high ductility was observed for both silk micropillars and hollow nanopillars as shown separately in Figure 14E and Figure 14F. Such a high ductility has never been reported for dried silk materials. Polymeric materials are known to exhibit a length scale-dependent mechanical behavior such as large ductility in low-dimensional structures.[37] Similar phenomenon might be at play for silk micro- and nanostructures studied here. The possible reason for such length-scale dependent mechanical properties is the enhanced polymer chain mobility at the surface due to the significantly lower entanglement density at the surface compared to the bulk. However, a more detailed study focused on the thermomechanical properties (*e.g.*, depression in glass transition temperature) of silk films with different thickness can provide more insight into the mechanistic aspects of the length scale-dependent mechanical behavior.

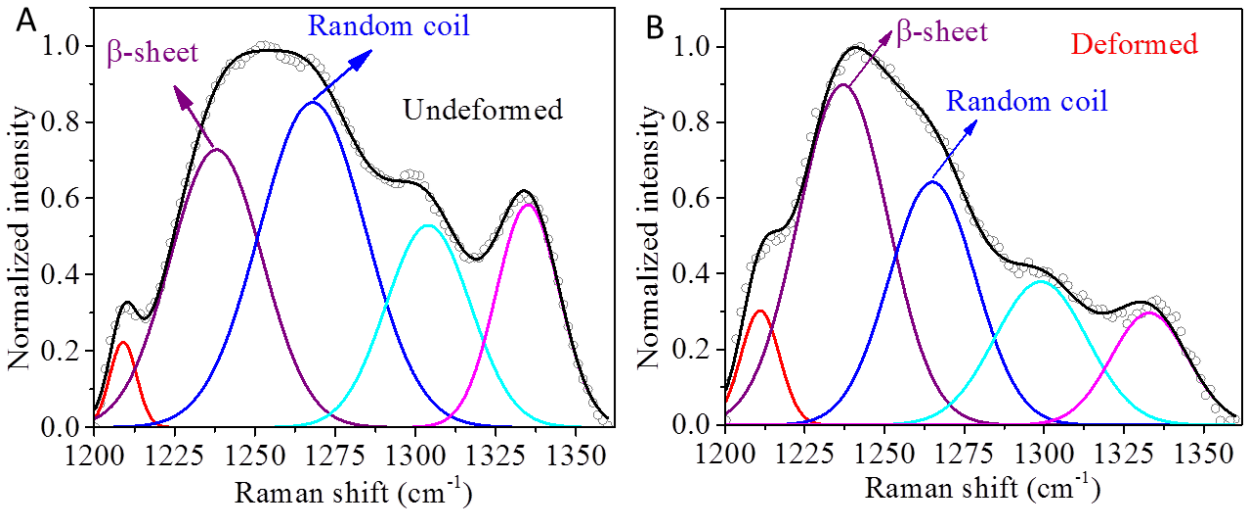

Figure 15: (B) Raman spectra of silk stripes from undeformed and necked regions. Zoom-in of the amide III Raman band from (A) undeformed and (B) necked regions with deconvoluted peaks.

To uncover secondary structure changes in deformed silk stripes, the Raman spectrum in amide III region of Figure 11B was deconvoluted into five Gaussian peaks (Figure 15A, B). In the undeformed regions, the most intense band was found to be at 1264 cm^{-1}, which corresponds to random coil and α-helical secondary structures of silk chains (Figure 15A). On the other hand, in the necked regions, the most intense peak occurred at 1231 cm^{-1}, indicative of anti-parallel β-sheet structures (Figure 15B). Furthermore, the amide I peak at 1660 cm^{-1}, corresponding to C=O stretching, was found to be sharper.[38] Although the spin-coating process may induce a change in the secondary structure silk (from silk I to silk II), this transition is confined to the thin interfacial regions (< 5 nm at substrate-film interface).[24] Such transition from silk I to silk II has been successfully employed to fabricate silk-on-silk ultrathin films, microcapsules and interfacial coatings using spin-assisted layer-by-layer assembly.[24] Beyond the substrate-film interfacial region, the spin-coated film exhibits primarily a silk I structure as evidenced by the Raman spectra of undeformed stripe segments, which are rich in random coil and α-helical secondary structures (Figure 15A). However, Figure 15B showed that the locally necked stripe segments were dominated by silk II, suggesting that the transition of silk secondary structures from silk I to silk II occurred indeed during stretching.

We have demonstrated facile methods to fabricate low-dimensional patterned silk films and silk micro/nanopillars. The successful transfer of the patterned silk films to stretchable substrates without using any organic solvent enabled us to investigate the relationship between their secondary structures and mechanical properties starting with native conformation. These low-dimensional silk materials showed extremely high local ductility that critically depended on the secondary structures. Strain induced conformation transition was observed in dry reconstituted silk materials at the micro/nanoscale. These results may provide insights into structure-function relationship of silk materials at micro and nanoscale, and hold promise for applications in tissue engineering, controlled drug delivery and release, electronic and optical devices. The elastoplastic deformation and length-scale dependent mechanical properties of silk fibroin can be harnessed to overcome the brittle nature of reconstituted silk structures through the careful design of the load bearing elements.

Peer-reviewed publications with AFOSR support: Current AFOSR project (06/2015 - 06/2018) resulted in very exciting results, which were widely disseminated, presented at numerous conferences, and published in top-ranked archival journals. Total, 21 refereed publications resulted from this support (see a list of papers below). Three Front Covers in Advanced Materials Interfaces (2016), *Advanced Materials* (2017) and *Chemical Reviews* (2017) highlighted the results from current project. Invited reviews on related topics have been published in *Chemical Reviews,* 2017. The PI and Dr. Rajesh Naik from Air Force Research Lab have guest co-edited a special issue titled "Bioinspired and Biomimetic Optical Materials" covering topics closely related to the current project. The publications resulting from the current project are listed below and the names of the collaborators from Air Force Research Laboratory are underlined.

Publications from AFOSR support

1) "Flexible solid-state supercapacitor based on tin oxide/reduced graphene oxide/bacterial nanocellulose" Liu, KK.; Jiang, Q.; Kacica, C.; Derami, H.; Biswas, P.; Singamaneni, S. *RSC Advances,* **2018**, *8*, 31296.
2) "Ultra-robust Biochips with Metal-Organic Framework Coatings for Point-of-Care Diagnosis" Wang, C.; Wang, L.; Tadepalli, S.; Morrissey, J.; Kharasch, E.; Naik, R. R.; Singamaneni, S. *ACS Sensors* **2018**, *3*, 342-351.
3) "Metal-Organic Framework Encapsulation for Biospecimen Preservation" Wang, C.; Sun, H.; Luan, J.; Jiang, Q.; Tadepalli, S.; Morrissey, J. J.; Kharasch, E. D.; Singamaneni, S. *Chem. Mater.* **2018**, *30*, 1291-1300.
4) "Catalytically Active Bacterial Nanocellulose-Based Ultrafiltration Membrane" Xu, T.; Jiang, Q.; Ghim, D.; Liu, KK.; Sun, H.; Derami, H.G.; Wang, Z.; Tadepalli, S.; Jun, YS.; Zhang, Q.; Singamaneni, S. *Small.* ***2018***, 14, 1704006.
5) "Extreme Mechanical Behavior of Nacre-Mimetic Graphene-Oxide and Silk Nanocomposite" Xie, W.; Tadepalli, S. ; Park, S.- H.; Kazemi M. A.; Jiang, Q.; Singamaneni, S.; Lee, J.-H. *Nano. Lett.* **2018**, *18*, 987-993
6) "Metal-Organic Framework Encapsulation for the Preservation and Photothermal Enhancement of Enzyme Activity." Tadepalli, S.; Yim, J.; Cao, S.; Naik, R. R.; Singamaneni, S. *Small*, **2018**, 1702382.
7) "Effect of Size and Curvature on the Enzyme Activity of Bionanoconjugates." Tadepalli, S.; Wang, Z.; Slocik, J. M.; Naik, R. R.; Singamaneni, S.; *Nanoscale.* **2017**, *9*, 15666-15672.
8) "Gold Nanorod-mediated Photothermal Enhancement of Biocatalytic Activity of Polymer Encapsulated Enzyme" Tadepalli, S.; Yim, J.; Madireddi, K.; Luan, J.; Naik, R.R.; Singamaneni, S. *Chem. Mater.* **2017**, *29*, 6308-6314
9) "Influence of Surface Charge of the Nanostructures on the Biocatalytic Activity" Tadepalli, S.; Wang, Z.; Liu, K.-K.; Jiang, Q.; Slocik, J. M.; Naik, R. R.; Singamaneni S. *Langmuir* **2017**, *33*, 6611-6619.
10) "Bio-optics and Bioinspired Optical Materials." Tadepalli, S.; Gupta, M.; Slocik, J. M; Naik. R. R.; Singamaneni, S. *Chem. Rev.,* **2017***, 117*, 12705–12763. (Featured on the cover)

11) “Metal-Organic Framework as Protective Coating for Biodiagnostic Chips” Wang, C.; Tadepalli, S.; Luan, J.; Liu, K.-K.; Morrissey, J.; Kharasch, E.; Naik, R.R.; Singamaneni, S. *Adv. Mater.* **2017**, *29*, 1604433.
12) “Wood-Graphene oxide Composite for Highly Efficient Solar Steam Generation and Desalination” Liu K.-K.; Jiang, Q.; Tadepalli, S.; Raliya, R.; Biswas, P.; Naik, R. R.; Singamaneni, S. *ACS Appl. Mater. Interfaces* **2017**, *9*, 7675-7681
13) “Silk-Encapsulated Plasmonic Biochips with Enhanced Thermal Stability” Wang, C.; Luan, J.; Tadepalli, S.; Liu, K.-K.; Morrissey, J.; Kharasch, E.; Naik, R. R.; Singamaneni, S. *ACS Appl. Mater. Interfaces* **2016**, *8*, 26493-26500.
14) “Bilayered Biofoam for Highly Efficient Solar Steam Generation” Jiang, Q.; Tian, L.; Liu, K.-K.; Tadepalli, S.; Raliya, R.; Biswas, P.; Naik, R. R.; Singamaneni, S. *Adv. Mater.* **2016**, *42*, 9400-9407.
15) “Adsorption Behavior of Silk Fibroin on Amphiphilic Graphene Oxide” Tadepalli, S.; Hamper, H.; Park, S. H.; Cao, S.; Naik, R. R.; Singamaneni, S. *ACS Biomat. Sci. Engg.* **2016**, *2*, 1084-1092.
16) “Elastoplastic Deformation of Silk Micro and Nanostructures" Huang, G.; Tian, L.; Liu, K.-K.; Hu, B.; Xu, F.; Lu, T. J.; Naik, R.R.; Singamaneni, S. *ACS Biomat. Sci. Engg.* **2016**, *2*, 893-899.
17) “Bacterial Nanocellulose-based Flexible Surface Enhanced Raman Scattering Substrate” Tian, L.; Jiang, Q.; Liu, K.-K.; Luan, J.; Naik, R. R.; Singamaneni, S. *Adv. Mater. Interfaces* **2016**, 3: 1600214.
18) “Plasmonic Nanogels for Unclonable Optical Tagging” Tian, L.; Liu, K.-K.; Fei, M.; Tadepalli, S.; Cao, S.; Geldmeier, J.; Tsukruk, V.; Singamaneni, S. *ACS Appl. Mater. Interfaces* **2016**, 8, 4031-4041
19) “Plasmonic Paper: A Porous and Flexible Substrate Enabling Nanoparticle-Based Combinatorial Chemistry” Schmucker, A.; Tadepalli, S.; Liu, K-.K.; Sullivan, C.; Singamaneni, S.; Naik, R. R. *RSC Advances* **2016**, *6*, 4136-4144.
20) “Plasmonic Biofoam: A Versatile Optically-active Material” Tian, L; Luan, J; Liu, K.-K.; Jiang, Q.; Tadepalli, S.; Gupta, M.; Naik, R. R.; Singamaneni, S. *Nano Lett.* **2016**, *16*, 609-616.
21) “Peptide Functionalized Gold Nanorods for the Sensitive Detection of a Cardiac Biomarker Using Plasmonic Paper Devices” Tadepalli, S.; Kuang, Z.; Jiang, Q.; Liu, K.-K.; Fisher, M. A.; Morrissey, J. J.; Kharasch, E. D.; Sloick, J. M., Naik, R.R.; Singamaneni, S. **2015**, *5*, 16206.

Personnel training and collaboration with AFRL researchers

Materials Science graduate students, who participated in the project and graduated in the past three years are: Dr. Sirimuvva Tadepalli (PhD, 2017, a post-doc fellow at Stanford U.); Dr. Keng-Ku Liu (PhD, 2017, Research Scientist, Auragent Bioscience, St. Louis). The project also partially supported a postdoctoral researcher in the PI’s lab (Dr. C. Wang, soon to start as an assistant professor at South Dakota University Mines and Technology). In 2015-2018, PI’s students received a number of prestigious awards and fellowships including **2017 MRS Gold Award** for Graduate Student Research (the highest national distinction in materials, S. Tadepalli). The study immensely benefited from intense collaboration with AFRL researchers facilitated by mutual visits of PI and AFRL researchers (Dr. R. Naik, Dr. A. Schmucker, Dr. J. Slocik, and Dr. M. Gupta). The collaboration with AFRL researchers included biomolecules supply (peptides, suckerin protein) and SPR and CD studies at Dr. R. Naik’s group (15 joint refereed publications within last three years).

References

1. Zhang, J.; Zhang, F.; Yang, H.; Huang, X.; Liu, H.; Zhang, J.; Guo, S., Graphene Oxide as a Matrix for Enzyme Immobilization. *Langmuir* **2010,** *26* (9), 6083-6085.
2. Ugarova, N. N.; Rozhkova, G. D.; Berezin, I. V., Chemical modification of the ε-amino groups of lysine residues in horseradish peroxidase and its effect on the catalytic properties and thermostability of the enzyme. *Biochimica et Biophysica Acta (BBA) - Enzymology* **1979,** *570* (1), 31-42.
3. Sanfins, E.; Augustsson, C.; Dahlbäck, B.; Linse, S.; Cedervall, T., Size-Dependent Effects of Nanoparticles on Enzymes in the Blood Coagulation Cascade. *Nano Letters* **2014,** *14* (8), 4736-4744.
4. Berglund, G. I.; Carlsson, G. H.; Smith, A. T.; Szoke, H.; Henriksen, A.; Hajdu, J., The catalytic pathway of horseradish peroxidase at high resolution. *Nature* **2002,** *417* (6887), 463-468.
5. Sanfins, E.; Augustsson, C.; Dahlbäck, B.; Linse, S.; Cedervall, T., Size-Dependent Effects of Nanoparticles on Enzymes in the Blood Coagulation Cascade. *Nano Lett.* **2014,** *14* (8), 4736-4744.
6. Berg, J.; Tymoczko, J.; Stryer, L., The Michaelis-Menten Model Accounts for the Kinetic Properties of Many Enzymes. *Biochemistry* **2002,** *5th edition* (Section 8.4).
7. Wu, C.-S.; Lee, C.-C.; Wu, C.-T.; Yang, Y.-S.; Ko, F.-H., Size-modulated catalytic activity of enzyme-nanoparticle conjugates: a combined kinetic and theoretical study. *Chem. Commun.* **2011,** *47* (26), 7446-7448.
8. Tian, L.; Tadepalli, S.; Fei, M.; Morrissey, J. J.; Kharasch, E. D.; Singamaneni, S., Off-Resonant Gold Superstructures as Ultrabright Minimally Invasive Surface-Enhanced Raman Scattering (SERS) Probes. *Chem. Mater* **2015,** *27* (16), 5678-5684.
9. Tian, L.; Fei, M.; Tadepalli, S.; Morrissey, J. J.; Kharasch, E. D.; Singamaneni, S., Bio-Enabled Gold Superstructures with Built-In and Accessible Electromagnetic Hotspots. *Adv Healthc Mater* **2015,** *4* (10), 1502-1509.
10. Orendorff, C. J.; Gearheart, L.; Jana, N. R.; Murphy, C. J., Aspect ratio dependence on surface enhanced Raman scattering using silver and gold nanorod substrates. *Physical Chemistry Chemical Physics* **2006,** *8* (1), 165-170.
11. Abbas, A.; Tian, L.; Morrissey, J. J.; Kharasch, E. D.; Singamaneni, S., Hot Spot-Localized Artificial Antibodies for Label-Free Plasmonic Biosensing. *Advanced Functional Materials* **2013,** *23* (14), 1789-1797.
12. Correro, M. R.; Moridi, N.; Schützinger, H.; Sykora, S.; Ammann, E. M.; Peters, E. H.; Dudal, Y.; Corvini, P. F. X.; Shahgaldian, P., Enzyme Shielding in an Enzyme-thin and Soft Organosilica Layer. *Angewandte Chemie International Edition* **2016,** *55* (21), 6285-6289.
13. Luan, J.; Liu, K.-K.; Tadepalli, S.; Jiang, Q.; Morrissey, J. J.; Kharasch, E. D.; Singamaneni, S., PEGylated Artificial Antibodies: Plasmonic Biosensors with Improved Selectivity. *ACS Applied Materials & Interfaces* **2016,** *8* (36), 23509-23516.
14. Jain, P. K.; Huang, X.; El-Sayed, I. H.; El-Sayed, M. A., Noble Metals on the Nanoscale: Optical and Photothermal Properties and Some Applications in Imaging, Sensing, Biology, and Medicine. *Accounts of Chemical Research* **2008,** *41* (12), 1578-1586.
15. Bretschneider, J. C.; Reismann, M.; von Plessen, G.; Simon, U., Photothermal Control of the Activity of HRP-Functionalized Gold Nanoparticles. *Small* **2009,** *5* (22), 2549-2553.
16. Kuzuhara, A.; Asakura, T.; Tomoda, R.; Matsunaga, T., Use of silk fibroin for enzyme membrane. *J. Biotechnol.* **1987,** *5* (3), 199-207.
17. Hu, K.; Gupta, M. K.; Kulkarni, D. D.; Tsukruk, V. V., Ultra-Robust Graphene Oxide-Silk Fibroin Nanocomposite Membranes. *Adv. Mater.* **2013,** *25* (16), 2301-2307.
18. Zhang, C.; Song, D.; Lu, Q.; Hu, X.; Kaplan, D. L.; Zhu, H., Flexibility Regeneration of Silk Fibroin in Vitro. *Biomacromolecules* **2012,** *13* (7), 2148-2153.
19. Jin, H. J.; Park, J.; Karageorgiou, V.; Kim, U. J.; Valluzzi, R.; Cebe, P.; Kaplan, D. L., Water-Stable Silk Films with Reduced β-Sheet Content. *Adv. Funct. Mater.* **2005,** *15* (8), 1241-1247.
20. Hu, X.; Kaplan, D.; Cebe, P., Determining Beta-Sheet Crystallinity in Fibrous Proteins by Thermal Analysis and Infrared Spectroscopy. *Macromolecules* **2006,** *39* (18), 6161-6170.

21. Partlow, B. P.; Hanna, C. W.; Rnjak-Kovacina, J.; Moreau, J. E.; Applegate, M. B.; Burke, K. A.; Marelli, B.; Mitropoulos, A. N.; Omenetto, F. G.; Kaplan, D. L., Highly Tunable Elastomeric Silk Biomaterials. *Adv. Funct. Mater.* **2014,** *24* (29), 4615-4624.
22. Litvinov, Rustem I.; Faizullin, Dzhigangir A.; Zuev, Yuriy F.; Weisel, John W., The α-Helix to β-Sheet Transition in Stretched and Compressed Hydrated Fibrin Clots. *Biophys. J.* **2012,** *103* (5), 1020-1027.
23. Perrone, G. S.; Leisk, G. G.; Lo, T. J.; Moreau, J. E.; Haas, D. S.; Papenburg, B. J.; Golden, E. B.; Partlow, B. P.; Fox, S. E.; Ibrahim, A. M. S.; Lin, S. J.; Kaplan, D. L., The use of silk-based devices for fracture fixation. *Nat Commun* **2014,** *5*.
24. Jiang, C.; Wang, X.; Gunawidjaja, R.; Lin, Y. H.; Gupta, M. K.; Kaplan, D. L.; Naik, R. R.; Tsukruk, V. V., Mechanical Properties of Robust Ultrathin Silk Fibroin Films. *Adv. Funct. Mater.* **2007,** *17* (13), 2229-2237.
25. Jin, H.-J.; Park, J.; Valluzi, R.; Kim, U.-J.; Cebe, P.; Kaplan, D., Bioprocessing of silk proteins-controlling assembly. In *Bionanotechnology*, Renugopalakrishnan, V.; Lewis, R., Eds. Springer Netherlands: 2006; pp 189-208.
26. Ishida, M.; Asakura, T.; Yokoi, M.; Saito, H., Solvent- and mechanical-treatment-induced conformational transition of silk fibroins studies by high-resolution solid-state carbon-13 NMR spectroscopy. *Macromolecules* **1990,** *23* (1), 88-94.
27. Wilson, D.; Valluzzi, R.; Kaplan, D., Conformational Transitions in Model Silk Peptides. *Biophys. J.* **2000,** *78* (5), 2690-2701.
28. Gatenholm, P.; Klemm, D., Bacterial Nanocellulose as a Renewable Material for Biomedical Applications. *Mrs Bull* **2010,** *35* (3), 208-213.
29. Yamanaka, S.; Watanabe, K.; Kitamura, N.; Iguchi, M.; Mitsuhashi, S.; Nishi, Y.; Uryu, M., The structure and mechanical properties of sheets prepared from bacterial cellulose. *J Mater Sci* **1989,** *24* (9), 3141-3145.
30. Salmon, S.; Hudson, S. M., Crystal morphology, biosynthesis, and physical assembly of cellulose, chitin, and chitosan. *Journal of Macromolecular Science, Part C: Polymer Reviews* **1997,** *37* (2), 199-276.
31. Jin, H.; Nishiyama, Y.; Wada, M.; Kuga, S., Nanofibrillar cellulose aerogels. *Colloids and Surfaces A: Physicochemical and Engineering Aspects* **2004,** *240* (1–3), 63-67.
32. Klemm, D.; Kramer, F.; Moritz, S.; Lindström, T.; Ankerfors, M.; Gray, D.; Dorris, A., Nanocelluloses: A New Family of Nature-Based Materials. *Angewandte Chemie International Edition* **2011,** *50* (24), 5438-5466.
33. Valo, H.; Arola, S.; Laaksonen, P.; Torkkeli, M.; Peltonen, L.; Linder, M. B.; Serimaa, R.; Kuga, S.; Hirvonen, J.; Laaksonen, T., Drug release from nanoparticles embedded in four different nanofibrillar cellulose aerogels. *European Journal of Pharmaceutical Sciences* **2013,** *50* (1), 69-77.
34. Falk, L.; Emmerich, H.; Antje, P.; Dieter, L.; Stefanie, T.; Marie-Alexandra, N.; Martin, W.; Thomas, R., Cellulosic aerogels as ultra-lightweight materials. Part 2: Synthesis and properties 2ndICC 2007, Tokyo, Japan, October 25–29, 2007. *Holzforschung: International Journal of the Biology, Chemistry, Physics, & Technology of Wood* **2009,** *63* (1), 3-11.
35. Huang, X. H.; Neretina, S.; El-Sayed, M. A., Gold Nanorods: From Synthesis and Properties to Biological and Biomedical Applications. *Advanced Materials* **2009,** *21* (48), 4880-4910.
36. Tian, L.; Chen, E.; Gandra, N.; Abbas, A.; Singamaneni, S., Gold Nanorods as Plasmonic Nanotransducers: Distance-Dependent Refractive Index Sensitivity. *Langmuir* **2012,** *28* (50), 17435-17442.
37. Jang, J. H.; Ullal, C. K.; Choi, T. Y.; Lemieux, M. C.; Tsukruk, V. V.; Thomas, E. L., 3D polymer microframes that exploit length-scale-dependent mechanical behavior. *Adv. Mater.* **2006,** *18* (16), 2123-2127.
38. Gupta, M. K.; Singamaneni, S.; McConney, M.; Drummy, L. F.; Naik, R. R.; Tsukruk, V. V., A facile fabrication strategy for patterning protein chain conformation in silk materials. *Adv. Mater.* **2010,** *22* (1), 115-119.